The Astrophysical Journal, 999:227 (26pp), 2026 March 10 https://doi.org/10.3847/1538-4357/ae4318

Photometry and Spectroscopy of SN 2024pxl: A Luminosity Link among Type Iax Supernovae

Mridweeka Singh[1], Lindsey A. Kwok[2,58], Saurabh W. Jha[3], R. Dastidar[4], Conor Larison[3], Alexei V. Filippenko[5], Jennifer E. Andrews[6], Moira Andrews[7,8], G. C. Anupama[1], Prasiddha Arunachalam[9], Katie Auchettl[9,10], Dominik Bánhidi[11,12], Barnabas Barna[11], K. Azalee Bostroem[13,59], Thomas G. Brink[5], Régis Cartier[14], Ping Chen[15,16], Collin T. Christy[13], David A. Coulter[17], Sofia Covarrubias[18], Kyle W. Davis[9], Connor B. Dickinson[9], Yize Dong[19], Joseph Farah[7,8], Andreas Flörs[20], Ryan J. Foley[9], Noah Franz[13], Christoffer Fremling[18,21], Lluís Galbany[22,23], Anjasha Gangopadhyay[24], Aarna Garg[9], Elinor L. Gates[25], Or Graur[26,27], Alexa C. Gordon[2,28], Daichi Hiramatsu[19,29], Emily Hoang[30], D. Andrew Howell[7,8], Brian Hsu[13], Joel Johansson[31], Arti Joshi[32], Lordrick A. Kahinga[9], Ravjit Kaur[9], Sahana Kumar[33], Piramon Kumnurdmanee[9], Hanindyo Kuncarayakti[34,35], Natalie LeBaron[5], C. Lidman[36,37], Chang Liu[2,28], Keiichi Maeda[38], Kate Maguire[39], Bailey Martin[36], Curtis McCully[7,8], Darshana Mehta[30], Luca M. Menotti[9], Anne J. Metevier[40], A. A. Miller[2,28,41], Kuntal Misra[42], C. Tanner Murphey[43,44,45], Megan Newsome[7,46], Estefania Padilla Gonzalez[47], Kishore C. Patra[9], Jeniveve Pearson[13], Anthony L. Piro[48], Abigail Polin[49], Aravind P. Ravi[30], Armin Rest[17,47], Nabeel Rehemtulla[2,28,41], Nicolas Meza Retamal[30], O. M. Robinson[9], César Rojas-Bravo[9], Devendra K. Sahu[1], David J. Sand[13], Brian P. Schmidt[36], Steve Schulze[2], Michaela Schwab[3], Manisha Shrestha[13], Matthew R. Siebert[17], Sunil Simha[2,50], Nathan Smith[13], Jesper Sollerman[24], Shubham Srivastav[51], Bhagya M. Subrayan[13], Tamás Szalai[11,52], Kirsty Taggart[9], Rishabh Singh Teja[1], Jacco H. Terwel[39,53], Samaporn Tinyanont[54], Stefano Valenti[30], József Vinkó[11,46,55,56], Aya L. Westerling[9], J. Craig Wheeler[46], Yi Yang[5,57], and WeiKang Zheng[5]

[1] Indian Institute of Astrophysics, Koramangala 2nd Block, Bangalore 560034, India; mridweeka.singh@iiap.res.in, yashasvi04@gmail.com
[2] Center for Interdisciplinary Exploration and Research in Astrophysics (CIERA), 1800 Sherman Avenue, Evanston, IL 60201, USA
[3] Department of Physics and Astronomy, Rutgers, The State University of New Jersey, 136 Frelinghuysen Road, Piscataway, NJ 08854-8019, USA
[4] Istituto Nazionale di Astrofisica, Osservatorio Astronomico di Brera, via E. Bianchi 46, 23807 Merate (LC), Italy
[5] Department of Astronomy, University of California, Berkeley, CA 94720-3411, USA
[6] Gemini Observatory/NSF's NOIRLab, 670 North A'ohoku Place, Hilo, HI 96720-2700, USA
[7] Las Cumbres Observatory, 6740 Cortona Drive, Suite 102, Goleta, CA 93117-5575, USA
[8] Department of Physics, University of California, Santa Barbara, CA 93106-9530, USA
[9] Department of Astronomy and Astrophysics, University of California, Santa Cruz, CA 95064-1077, USA
[10] School of Physics, The University of Melbourne, Parkville, VIC 3010, Australia
[11] Department of Experimental Physics, Institute of Physics, University of Szeged, Dóm tér 9, 6720 Szeged, Hungary
[12] Baja Astronomical Observatory of the University of Szeged, Szegedi út, Kt. 766, 6500 Baja, Hungary
[13] Steward Observatory, University of Arizona, 933 North Cherry Avenue, Tucson, AZ 85721-0065, USA
[14] Centro de Astronomía (CITEVA), Universidad de Antofagasta, Av. Angamos 601, Antofagasta, Chile
[15] Institute for Advanced Study in Physics, Zhejiang University, Hangzhou 310027, People's Republic of China
[16] Department of Particle Physics and Astrophysics, Weizmann Institute of Science, 76100 Rehovot, Israel
[17] Space Telescope Science Institute, 3700 San Martin Drive, Baltimore, MD 21218-2410, USA
[18] Division of Physics, Mathematics and Astronomy, California Institute of Technology, Pasadena, CA 91125, USA
[19] Center for Astrophysics | Harvard & Smithsonian, 60 Garden Street, Cambridge, MA 02138-1516, USA
[20] GSI Helmholtzzentrum für Schwerionenforschung, Planckstraße 1, 64291 Darmstadt, Germany
[21] Caltech Optical Observatories, California Institute of Technology, Pasadena, CA 91125, USA
[22] Institute of Space Sciences (ICE, CSIC), Campus UAB, Carrer de Can Magrans, s/n, E-08193 Barcelona, Spain
[23] Institut d'Estudis Espacials de Catalunya (IEEC), E-08034 Barcelona, Spain
[24] Department of Astronomy, Oskar Klein Center, Stockholm University, SE-106 91 Stockholm, Sweden
[25] UCO/Lick Observatory, PO Box 85, Mount Hamilton, CA 95140, USA
[26] Institute of Cosmology and Gravitation, University of Portsmouth, Dennis Sciama Building, Burnaby Road, Portsmouth PO1 3FX, UK
[27] Department of Astrophysics, American Museum of Natural History, Central Park West and 79th Street, New York, NY 10024-5192, USA
[28] Department of Physics and Astronomy, Northwestern University, 2145 Sheridan Road, Evanston, IL 60208, USA
[29] The NSF AI Institute for Artificial Intelligence and Fundamental Interactions, Cambridge, MA 02139, USA
[30] Department of Physics and Astronomy, University of California, Davis, 1 Shields Avenue, Davis, CA 95616-5270, USA
[31] Department of Physics, Oskar Klein Centre, Stockholm University, SE-106 91, Stockholm, Sweden
[32] Instituto de Astrofísica, Facultad de Física, Pontificia Universidad Católica de Chile, Av. Vicuña Mackenna 4860, Santiago, Chile
[33] Department of Astronomy, University of Virginia, 530 McCormick Road, Charlottesville, VA 22904, USA
[34] Tuorla Observatory, Department of Physics and Astronomy, FI-2001, University of Turku, Finland
[35] Finnish Centre for Astronomy with ESO (FINCA), FI-20014, University of Turku, Finland
[36] Research School of Astronomy and Astrophysics, Australian National University, Canberra, ACT 2611, Australia
[37] Centre for Gravitational Astrophysics, College of Science, Australian National University, ACT 2601, Australia
[38] Department of Astronomy, Kyoto University, Kitashirakawa-Oiwake-cho, Sakyo-ku, Kyoto, 606-8502, Japan
[39] School of Physics, Trinity College Dublin, The University of Dublin, Dublin 2, Ireland
[40] University of California Observatories, 550 Red Hill Road, Santa Cruz, CA 95064, USA
[41] NSF-Simons AI Institute for the Sky (SkAI), 172 E. Chestnut Street, Chicago, IL 60611, USA
[42] Aryabhatta Research Institute of Observational Sciences (ARIES), Manora Peak, Nainital - 263001, India
[43] Department of Astronomy, University of Illinois, Urbana, IL 61801, USA
[44] Center for Astrophysical Surveys, National Center for Supercomputing Applications, Urbana, IL 61801, USA
[45] Illinois Center for Advanced Studies of the Universe, Urbana, IL 61801, USA
[46] Department of Astronomy, The University of Texas at Austin, 2515 Speedway, Stop C1400, Austin, TX 78712, USA

[47] Department of Physics and Astronomy, The Johns Hopkins University, 3400 North Charles Street, Baltimore, MD 21218, USA
[48] Observatories of the Carnegie Institute for Science, 813 Santa Barbara Street, Pasadena, CA 91101-1232, USA
[49] Department of Physics and Astronomy, Purdue University, 525 Northwestern Avenue, West Lafayette, IN 47907-2036, USA
[50] Department of Astronomy and Astrophysics, University of Chicago, William Eckhart Research Center, 5640 South Ellis Avenue, Chicago, IL 60637, USA
[51] Astrophysics sub-Department, Department of Physics, University of Oxford, Keble Road, Oxford, OX1 3RH, UK
[52] MTA-ELTE Lendület "Momentum" Milky Way Research Group, Szombathely, Szent Imre h. u. 112., H-9700, Hungary
[53] Nordic Optical Telescope, Rambla José Ana Fernández Pérez 7, ES-38711 Breña Baja, Spain
[54] National Astronomical Research Institute of Thailand, 260 Moo 4, Donkaew, Maerim, Chiang Mai 50180, Thailand
[55] Konkoly Observatory, HUN-REN Research Centre for Astronomy and Earth Sciences (CSFK), Konkoly-Thege Miklós út 15-17, 1121 Budapest, Hungary
[56] ELTE Eötvös Loránd University, Institute of Physics and Astronomy, Pázmány Péter sétány 1/A, Budapest, 1117, Hungary
[57] Physics Department and Tsinghua Center for Astrophysics, Tsinghua University, Beijing, 100084, People's Republic of China
Received 2025 May 5; revised 2026 February 2; accepted 2026 February 2; published 2026 March 9

Abstract

We present extensive ultraviolet to optical photometric and optical to near-infrared (NIR) spectroscopic follow-up observations of the nearby intermediate-luminosity ($M_V = -16.81 \pm 0.19$ mag) Type Iax supernovae (SNe Iax) 2024pxl in NGC 6384. SN 2024pxl exhibits a faster light curve than the high-luminosity members of this class, and slower than low-luminosity events. The observationally well-constrained rise time of ∼11 days and an estimated synthesized ^{56}Ni mass of 0.03 $M_\odot$, based on analytical modeling of the integrated spectral energy distribution light curve, are consistent with models of the weak deflagration of a carbon-oxygen white dwarf. Our optical spectral sequence of SN 2024pxl shows weak Si II lines and spectral evolution similar to other high-luminosity SNe Iax, but also a prominent early-time C II line, like lower-luminosity SNe Iax. The late-time optical spectrum of SN 2024pxl closely matches that of SN 2014dt, and its NIR spectral evolution aligns with that of other well-studied, high-luminosity SNe Iax. The spectral-line expansion velocities of SN 2024pxl are at the lower end of the SNe Iax velocity distribution, and the velocity distribution of iron-group elements compared to intermediate-mass elements suggests that the ejecta are mixed on large scales, as expected in pure deflagration models. SN 2024pxl exhibits characteristics intermediate between those of high-luminosity and low-luminosity SNe Iax, further establishing a link across this diverse class.

Unified Astronomy Thesaurus concepts: Supernovae (1668); Type Ia supernovae (1728)

Materials only available in the online version of record: data behind figures

1. Introduction

Type Iax supernovae (SNe Iax) are the fainter, peculiar cousins of Type Ia SNe (SNe Ia), both arising from the explosive thermonuclear fusion of carbon-oxygen (CO) white dwarfs (WDs; for a review, see S. W. Jha 2017). Owing to their homogeneity, "normal" SNe Ia serve as standardizable candles in cosmology (M. M. Phillips 1993; M. M. Phillips et al. 1999). SNe Iax), however, display comparatively lower luminosities, explosion energies, and ejecta velocities (A. V. Filippenko 2003; W. Li et al. 2003; R. J. Foley et al. 2013; S. W. Jha 2017). Their physical properties are also more heterogeneous, with luminosities ranging from $M_r = -12.7$ mag (V. R. Karambelkar et al. 2021) to $M_r = -18.6$ mag (M. D. Stritzinger et al. 2015), and line absorption velocities at maximum light between 2000 and 8000 km s^{-1} (R. J. Foley et al. 2009; M. D. Stritzinger et al. 2014). These distinct characteristics suggest that they arise from different progenitor systems and also have explosion mechanisms that differ in detail from those of normal SNe Ia.

The light curves of SNe Iax differ markedly from those of normal SNe Ia, rising faster and declining more rapidly in bluer bands (M. R. Magee et al. 2016, 2017; S. W. Jha 2017; L. Li et al. 2018). The light-curve-shape variations and the observed diversity in brightness (C. M. McClelland et al. 2010; G. Narayan et al. 2011; R. J. Foley et al. 2013; M. R. Magee et al. 2016; M. Singh et al. 2023) suggest that the synthesized ^{56}Ni, powering the light curve, spans a wide range from $8^{+4}_{-5} \times 10^{-4}$ $M_\odot$ (V. R. Karambelkar et al. 2021) to 0.3 $M_\odot$ (M. D. Stritzinger et al. 2015).

Spectroscopically, SNe Iax resemble 91T-like SNe Ia (M. M. Phillips et al. 2007) at early times, characterized by strong lines due to Fe III and Fe II and typically weak Si II. As they evolve, their late-time spectra diverge significantly from those of SNe Ia, displaying both permitted and forbidden lines of Fe and Ca (C. McCully et al. 2014a; M. D. Stritzinger et al. 2015). Notably, no fully nebular spectrum of a SNe Iax has been observed, owing to the persistence of lines with a pronounced P-Cygni profile for hundreds of days (e.g., Y. Camacho-Neves et al. 2023). Their spectral evolution slows considerably after 200−400 days past maximum light (R. J. Foley et al. 2016). K. Maeda & M. Kawabata (2022) discussed the existence of an Fe-rich innermost region and its association with a bound WD (remnant) using the day 500 spectrum of SN 2019muj.

High-luminosity and low-luminosity SNe Iax differ spectroscopically. For example, high-luminosity objects do not show a strong C II feature at 6580 Å, whereas low-luminosity ($M_V \gtrsim -15$ mag) SNe Iax do. Low-luminosity objects such as SNe 2008ha (R. J. Foley et al. 2009), 2010ae (M. D. Stritzinger et al. 2014), 2019gsc (S. Srivastav et al. 2020; L. Tomasella et al. 2020), 2020kyg (S. Srivastav et al. 2022; M. Singh et al. 2023), and 2021fcg (V. R. Karambelkar et al. 2021) also exhibit rapid spectroscopic evolution, lower expansion velocities, and a faster transition to the partial nebular phase.

Weak deflagrations of CO WDs are promising explosion models for SNe Iax, roughly reproducing many observed properties of brighter objects, such as their ^{56}Ni masses, peak

[58] CIERA Fellow.
[59] LSST-DA Catalyst Fellow.

luminosities, rise times, and early-time spectra (D. Branch et al. 2004; G. C. Jordan et al. 2012; M. Kromer et al. 2013; M. Fink et al. 2014; F. Lach et al. 2022). However, these models struggle to match low-luminosity SNe Iax that may instead be explained by weak deflagrations in hybrid carbon-oxygen-neon (CONe) WDs (X. Meng & P. Podsiadlowski 2014; M. Kromer et al. 2015).

SN 2012Z offered a valuable opportunity to investigate the progenitor systems of SNe Iax. Using deep Hubble Space Telescope (HST) pre-explosion images of its host galaxy NGC 1309, C. McCully et al. (2014b) detected a luminous blue source at the location of the SN and proposed a progenitor system consisting of a CO WD with a helium-star companion. Follow-up observations of SN 2012Z confirmed that the SN is still brighter than pre-explosion, suggesting that the helium-star companion survived the explosion and that a bound remnant was left behind (C. McCully et al. 2022; M. Schwab et al. 2026). A similar progenitor scenario was suggested for SN 2014dt (R. J. Foley et al. 2015). Moreover, a faint red source was identified in HST images taken 4 yr after the explosion of SN 2008ha that may be a companion star or remnant (R. J. Foley et al. 2014). In the case of SN 2020udy, another bright SNe Iax, constraints on interaction with a companion star from light curves obtained soon after the explosion also favor a helium-star companion (K. Maguire et al. 2023).

SN 2024pxl ($\alpha = 17^{\rm h}32^{\rm m}27\overset{\rm s}{.}350$, $\delta = +07^{\circ}03'44\overset{''}{.}68$, J2000) was first discovered and reported to the Transient Name Server[60] by the BTSbot machine-learning model (N. Rehemtulla et al. 2024b) on 2024 July 23 at 09:41:18 (UTC dates are used throughout this paper) using data from the Zwicky Transient Facility (ZTF; E. C. Bellm et al. 2019a, 2019b; M. J. Graham et al. 2019; F. J. Masci et al. 2019; R. Dekany et al. 2020). As part of the BTSbot-nearby program (N. Rehemtulla et al. 2025), BTSbot triggered a target-of-opportunity photometric and spectroscopic request to the SEDM spectrograph (N. Blagorodnova et al. 2018; Y. L. Kim et al. 2022). SN 2024pxl is located $45\overset{''}{.}5$ E and $7\overset{''}{.}8$ N from the nucleus of its host galaxy, NGC 6384. Other designations of this SN are ATLAS24lpk and ZTF24aawrofs. S. Smartt et al. (2024) classified SN 2024pxl as a SNe Iax, noting a strong resemblance to the bright SN Iax, SN 2005hk, 1 week before maximum light.

This study presents an extensive follow-up campaign of SN 2024pxl, integrating observations from both ground- and space-based telescopes. SN 2024pxl is perhaps the best-sampled SNe Iax to date in terms of its photometric and spectroscopic data. L. A. Kwok et al. (2025) analyze optical and near-infrared (NIR) spectra from this study together with mid-infrared (MIR) data from the James Webb Space Telescope (JWST), providing important clues about the explosion mechanism and progenitor system, complementing the results presented here. Section 2 details the observations and data reduction, and Section 3 describes the distance determination, line-of-sight extinction, and explosion epoch estimation. Section 4 presents the light curve, color evolution, and analytical modeling of the integrated spectral energy distribution (SED) light curve. In Section 5, we examine the spectral features and line-velocity evolution of SN 2024pxl and compare it with other well-studied SNe Iax. Section 6 summarizes the key findings of this study.

[60] https://www.wis-tns.org

2. Observations and Data Reduction

2.1. Photometry

A high-cadence dataset for SN 2024pxl was acquired with both ground- and space-based telescopes as part of an extensive photometric observing campaign initiated on the day of discovery. Photometry in *BgVri* bands was obtained through the Global Supernova Project (GSP) collaboration using the Las Cumbres Observatory (LCO; T. M. Brown et al. 2013) 0.4 and 1 m telescopes. Preprocessing, including bias correction and flat-fielding, was handled by the BANZAI pipeline (C. McCully et al. 2018). Further data reduction was carried out using lcogtsnpipe (S. Valenti et al. 2016), a photometric reduction pipeline that uses point-spread-function (PSF) photometry (P. B. Stetson 1987) to calculate zero-points, color terms, and extracted magnitudes. Photometry in *BV* bands is reported in Vega magnitudes (A. U. Landolt 1992), while *gri*-band data are presented in AB magnitudes (J. B. Oke & J. E. Gunn 1983), calibrated against Sloan Digital Sky Survey (SDSS) sources (J. A. Smith et al. 2002). Given the proximity of SN 2024pxl to its host galaxy, host contamination was mitigated by subtracting template images acquired on 2018 March 7—before the explosion. These templates, originally taken for SN 2017drh (which exploded in the same galaxy), were subtracted using the PyZOGY algorithm (B. Zackay et al. 2016; D. Guevel & G. Hosseinzadeh 2017), integrated within the lcogtsnpipe pipeline.

Additional imaging of SN 2024pxl was obtained in *BVri* bands with the 1 m Nickel telescope at Lick Observatory. The images were calibrated using bias and sky flat-field frames following standard procedures. PSF photometry was performed and calibrated relative to Pan-STARRS1 photometric standards (H. A. Flewelling et al. 2020).

Early-time photometric observations of SN 2024pxl were also obtained through the Distance Less Than 40 Mpc (DLT40) survey (L. Tartaglia et al. 2018), using the PROMPT-MO 0.4 m telescope operated via the Skynet Robotic Telescope Network (D. Reichart et al. 2005). These observations were carried out in a broad, unfiltered "Open" mode, and the resulting data were transformed to the SDSS *r* band following the calibration and reduction procedures described by L. Tartaglia et al. (2018).

Multiband photometry was further acquired using the 0.76 m Katzman Automatic Imaging Telescope (KAIT; A. V. Filippenko et al. 2001) at Lick Observatory in the *BVRI* bands. All images were reduced with a custom pipeline[61] described by M. Ganeshalingam et al. (2010) and B. E. Stahl et al. (2019). Host-galaxy contamination was removed via image subtraction, using a pre-explosion template obtained on 2018 June 22. PSF photometry was performed with DAOPHOT (P. B. Stetson 1987) from the IDL Astronomy User's Library.[62] Photometric calibration was achieved using local standard stars from the Pan-STARRS1 Surveys (E. Schlafly et al. 2012), with magnitudes transformed into the Landolt standard system (A. U. Landolt 1992) using the relations from J. L. Tonry et al. (2012).

[61] https://github.com/benstahl92/LOSSPhotPypeline
[62] http://idlastro.gsfc.nasa.gov/

In addition, observations of SN 2024pxl were conducted in the *uBVgri* bands using the Direct 4k × 4k camera on the 1 m Henrietta Swope telescope at Las Campanas Observatory, Chile. A full description of the data reduction procedure is provided by C. D. Kilpatrick et al. (2018).

SN 2024pxl was observed with the Dark Energy Camera (DECam) in the *griz* bands as part of the Young Supernova Experiment DECam (NOIRLab proposal ID: 2023A-237157). Data reduction, image differencing, and forced photometry were performed using `photpipe` (A. Rest et al. 2014). Templates included public DECam Local Volume Exploration Survey (A. Drlica-Wagner et al. 2021) pre-explosion images from 2023 September 9 (*g*, *r*) and 2023 April 7 (*z*), as well as a public Billion Lines Indexing in a Click (N. Kamennoff et al. 2012) image from 2018 April 13 (*i*).

SN 2024pxl was also observed in the *z* band with the RC 80 and BRC80 robotic telescopes at Piszkesteto station of Konkoly Observatory and at Baja Observatory of University of Szeged, Hungary (a complete *BgVriz* light curve will be presented by D. Banhidi et al. 2026, in preparation). The magnitudes were computed via aperture photometry and tied to Pan-STARRS photometry of local stars, including a color term in the transformation.

The multiband photometry from the different instruments is consistent within the quoted uncertainties, with no significant systematic offsets observed. Optical photometry of SN 2024pxl is presented in the data behind Figure 2.

The Neil Gehrels Swift Observatory (Swift; N. Gehrels et al. 2004) observed SN 2024pxl with its Ultra-Violet/Optical Telescope (UVOT; P. W. A. Roming et al. 2005) in both ultraviolet (UV) and optical filters. We reduced the UVOT images using the High-Energy Astrophysics Software (`HEASoft`).[63] A circular source region centered at the position of the SN with a radius of 3″ was used for aperture photometry. We measured the background contribution from a circular region (aperture radius of 5″) that is not contaminated by any other sources. Zero-points for photometry were chosen from A. A. Breeveld et al. (2010) with time-dependent sensitivity corrections updated in 2020. Table 3 details the photometric observations of SN 2024pxl collected by Swift.

2.2. Spectroscopy

2.2.1. Optical Spectra

We have compiled an extensive spectral dataset for SN 2024pxl using multiple ground-based telescopes in the optical and NIR domains. Spectra of SN 2024pxl obtained with the double beam spectrograph (DBSP; J. B. Oke & J. E. Gunn 1982) mounted on the 5 m Hale Telescope at Palomar Observatory were reduced using `DBSP-DRP` (M. S. Mandigo-Stoba et al. 2022a, 2022b) and `PypeIt` (J. X. Prochaska et al. 2020). Spectra acquired with the Wide Field Spectrograph (WiFeS; M. Dopita et al. 2007, 2010) on the Australian National University (ANU) 2.3 m telescope at Siding Spring Observatory were reduced with the data reduction pipeline `PyWiFeS` (M. J. Childress et al. 2014; A. Carr et al. 2024). Spectroscopic observations were also triggered with the FLOYDS spectrograph on the 2 m Faulkes Telescope North and South (FTN and FTS; T. M. Brown et al. 2013) through the GSP collaboration. The spectra were reduced with the `floydsspec`[64] pipeline, using standard reduction techniques.

Gemini IRAF[65] packages were used to reduce the spectra of SN 2024pxl from the Gemini Multi-Object Spectrograph mounted at Gemini North (GMOS-N; I. M. Hook et al. 2004) and Gemini South (GMOS-S) Observatories. Two spectra of SN 2024pxl were acquired using the SPectrograph for the Rapid Acquisition of Transients (SPRAT; A. S. Piascik et al. 2014), mounted on the Liverpool Telescope (LT; I. A. Steele et al. 2004). Reduction of the SPRAT spectra was carried out using the `SPRAT` pipeline.

SN 2024pxl was observed with the Robert Stobie Spectrograph (RSS) attached to the 9.2 m Southern African Large Telescope (SALT). All RSS spectra were reduced using a custom pipeline based on standard Pyraf (Science Software Branch at STScI 2012) routines and the `PySALT` package (S. M. Crawford et al. 2010).

A few spectra of SN 2024pxl were taken with the Low Resolution Spectrograph 2 (LRS2; T. S. Chonis et al. 2014) mounted on the Hobby–Eberly Telescope (HET; L. W. Ramsey et al. 1998) located at McDonald Observatory. LRS2 is a two-beam spectrograph covering the blue (LRS2-B) and the red (LRS2-R) part of the optical spectrum with an average resolution of $\lambda/\Delta\lambda \sim 1500$. The data were reduced by the `Panacea` pipeline.[66]

As part of our observing campaign, we have utilized the Hanle Faint Object Spectrograph and Camera (HFOSC) mounted on the Himalayan Chandra Telescope (HCT; T. P. Prabhu & G. C. Anupama 2010). The HCT spectra were reduced using standard IRAF routines.

SN 2024pxl was observed with Binospec on the MMT telescope (D. Fabricant et al. 2019); these spectra were reduced using the `Binospec` IDL pipeline (J. Kansky et al. 2019). A spectrum was taken with the Low Resolution Imaging Spectrometer (LRIS; J. B. Oke et al. 1995) on the Keck I 10 m telescope, which was reduced in a standard way using the `LPipe` pipeline (D. A. Perley 2019). Many spectra of SN 2024pxl were obtained with the Kast double spectrograph (J. S. Miller & R. P. S. Stone 1994) on the Shane 3 m telescope at Lick Observatory, either at low airmass or with the slit aligned along the parallactic angle to minimize the effects of atmospheric dispersion (A. V. Filippenko 1982). The reduction of all Kast spectra was performed following standard procedures[67,68] as outlined by M. R. Siebert et al. (2019) and J. M. Silverman et al. (2012).

In our observing campaign, we acquired data from the Gran Telescopio Canarias (GTC) with OSIRIS and EMIR, and reduced the spectra using a dedicated pipeline based on `PypeIt` (J. X. Prochaska et al. 2020, 2021; L. Galbany et al. 2025). `PypeIt` was also used to reduce the spectra of SN 2024pxl gathered with the 2.56 m Nordic Optical Telescope (NOT) deploying the Alhambra Faint Object Spectrograph and Camera (ALFOSC). We collected one spectrum of SN 2024pxl with the XShooter spectrograph mounted on the Very Large Telescope

[63] https://heasarc.gsfc.nasa.gov/docs/software/heasoft/

[64] https://www.authorea.com/users/598/articles/6566

[65] IRAF is distributed by the National Optical Astronomy Observatories, operated by the Association of Universities for Research in Astronomy, Inc., under a cooperative agreement with the National Science Foundation.

[66] https://github.com/grzeimann/Panacea

[67] https://github.com/msiebert1/UCSC_spectral_pipeline

[68] https://github.com/ishivvers/TheKastShiv

(J. Vernet et al. 2011); the EsoReflLex pipeline (W. Freudling et al. 2013), including the XShooter module, was used to reduce it.

The reduced spectra were scaled to the photometry of the corresponding epoch using a linear fit. All spectra were dereddened and corrected for host-galaxy redshift. A log of the spectroscopic observations of SN 2024pxl is given in Table 4.

2.2.2. NIR Spectra

The first NIR spectrum in our observing campaign of SN 2024pxl was obtained from Near-InfraRed Echellette Spectrometer (NIRES) on the Keck II 10 m telescope through the Keck Infrared Transient Survey (KITS) program and reduced using procedures outlined by S. Tinyanont et al. (2024). Two spectra were obtained by the Folded-port InfraRed Echellette Spectrograph (FIRE; R. A. Simcoe et al. 2013) mounted on the 6.5 m Magellan-Baade Telescope at Las Campanas Observatory in Chile, and reduced using the IDL pipeline firehose (R. A. Simcoe et al. 2013). NIR spectra of SN 2024pxl were acquired from the NASA InfraRed Facility Telescope (IRTF) using the SpeX spectrograph (J. T. Rayner et al. 2003). Data reduction of SpeX data was performed with Spextool and included tasks such as flat-fielding, wavelength calibration, background subtraction, and spectra extraction (M. C. Cushing et al. 2004).

We obtained two NIR spectra of SN 2024pxl with the Espectrógrafo Multiobjeto Infra-Rojo spectrograph (EMIR; F. Garzón et al. 2022) mounted on the GTC, which were reduced using a dedicated pipeline based on PyEMIR (S. Pascual et al. 2010; N. Cardiel et al. 2019). The Southern Astrophysical Research (SOAR) telescope, equipped with TripleSpec (E. Schlawin et al. 2014), was also deployed to obtain NIR spectra. Spectra acquired by SOAR were reduced using the IDL-based Spextool package (M. C. Cushing et al. 2004). All NIR observations for SN 2024pxl are reported in Table 5.

3. Distance, Extinction, and Explosion Epoch

SN 2024pxl is hosted by NGC 6384 at a spectroscopic redshift of $z = 0.0056$ (D. J. Lagattuta et al. 2013). Fortunately, a normal (though highly dust-extinguished) SN Ia with a well-sampled light curve from LCO and Lick Observatory, SN 2017drh, was also hosted by NGC 6384 (B. E. Stahl et al. 2019). We estimate the distance to SN 2017drh using BayeSN, a hierarchical Bayesian SN Ia light-curve model (K. S. Mandel et al. 2022; M. Grayling et al. 2024). SN 2017drh was located near the center of NGC 6384 and is significantly dust reddened, much more than SNe Ia typically used for cosmological analyzes. Thus, we favored using BayeSN because it explicitly models host-galaxy dust reddening and extinction separately from intrinsic SN spectral energy distribution (SED) variations, unlike alternatives like SALT2 (J. Guy et al. 2007) that aggregate intrinsic and extrinsic SN Ia color variations.

Using the BayeSN model trained by S. M. Ward et al. (2023), and assuming an $R_V = 3.1$ reddening law, fitting the light curve of SN 2017drh yields a distance modulus to NGC 6384 of $\mu = 31.81 \pm 0.11$ mag, which corresponds to a distance of 23.0 ± 2.0 Mpc that we adopt for our analysis of SN 2024pxl. The BayeSN fit to SN 2017drh results in a host-galaxy extinction of $A_V = 2.77 \pm 0.04$ mag, confirming the large amount of dust along the line of sight to SN 2017drh. We present the LCO photometry, BayeSN fit, and spectroscopic observations of SN 2017drh in the Appendix.

We also perform a BayeSN fit to SN 2017drh allowing R_V to vary, given that previous observations of heavily dust-extinguished SNe Ia sometimes indicate low R_V (N. Elias-Rosa et al. 2006, 2008; K. Krisciunas et al. 2006; K. Misra et al. 2008; X. Wang et al. 2008; R. Amanullah et al. 2015), possibly due to scattering effects in the surrounding medium or an atypical dust grain size distribution (L. Wang 2005; A. Goobar 2008; K. S. Kawabata et al. 2014; J. Gao et al. 2015; M. Bulla et al. 2018). In that case, we can recover a model fit for SN 2017drh with $R_V = 1.45$ and $A_V = 1.88 \pm 0.10$ mag that is nearly indistinguishable from the $R_V = 3.1$ model, but with almost 1 mag less total extinction and thus a larger distance modulus, $\mu = 32.70 \pm 0.14$ mag. This would imply a distance of 34.7 ± 2.3 Mpc, significantly farther than our adopted estimate. Unfortunately, owing to the lack of NIR data for SN 2017drh, we cannot break the degeneracy between A_V and R_V. We thus proceed with our distance estimate using $R_V = 3.1$, but caution that the lower R_V fit and increased distance would imply a factor of $\sim$2 change in the derived luminosity of SN 2024pxl. We note that these distances bracket the distance to SN 2017drh derived by W. B. Hoogendam et al. (2025) of 29 ± 5 Mpc using the SNooPy code (C. R. Burns et al. 2011).

The extinction experienced by SN 2024pxl due to the Milky Way in the direction of NGC 6384 is $A_V = 0.338$ mag, corresponding to $E(B-V) = 0.11$ mag (E. F. Schlafly & D. P. Finkbeiner 2011) and assuming $R_V = 3.1$. Estimating the host-galaxy extinction is more difficult because, unlike the normal SN Ia 2017drh, we do not have a standard model color for the diverse SNe Iax class. However, in our spectroscopic observations of SN 2024pxl, we note the presence of narrow interstellar Na I D absorption lines from both the Milky Way and NGC 6384, with approximately equal strength. Thus, we crudely infer the host-galaxy contribution to the extinction of SN 2024pxl to be similar to the Milky Way extinction and adopt a total reddening and extinction along the line of sight to SN 2024pxl of $E(B-V) = 0.22$ mag and $A_V = 0.68$ mag.

A nondetection of SN 2024pxl was reported on 2024 July 21 (JD = 2460512.75; N. Rehemtulla et al. 2024a) with a limiting AB magnitude of 19.37 (3σ upper limit) in the r filter. To estimate the explosion epoch of SN 2024pxl, we combined photometric data from the ATLAS and ZTF surveys in four optical bands (ATLAS c and o; ZTF g and r). A power-law model of the form

$$F(t) = A \times (t - t_{\rm exp})^n , \quad (1)$$

was used to fit the early-time flux evolution, where A is a band-dependent scaling constant, $t_{\rm exp}$ is the explosion time, and n is the power-law index.

The model was simultaneously fit to all the observed fluxes in different bands (Figure 1). Unlike the commonly adopted fixed $n = 2$ assumption used in early light-curve fits to model a homologously expanding fireball (e.g., W. D. Arnett 1982; P. E. Nugent et al. 2011), we allowed n to vary as a free parameter to account for deviations observed in some thermonuclear SN subclasses (e.g., M. R. Magee et al. 2016). The best-fit result yields a common explosion epoch of

$$t_{\rm exp} = \text{JD } 2,460,514.36 \pm 0.10,$$

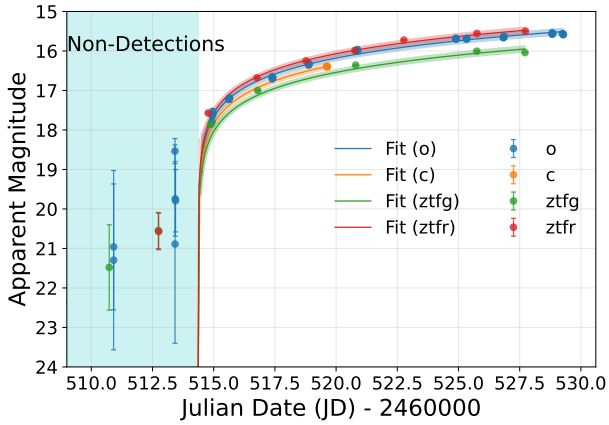

Figure 1. A power-law fit to the early-time photometry of SN 2024pxl in ATLAS *cyan*, *orange*, and ZTF *g* and *r* filters. Nondetections are indicated in the shaded region.

with a power-law index of

$$n = 0.634 \pm 0.019,$$

indicating a shallower rise than the typical $n = 2$ case. We emphasize that the quoted ± 0.10 day represents the formal statistical uncertainty from the power-law fit. In practice, the first detection occurs 0.96 day after this fitted zero-point, underscoring that the true uncertainty is significantly larger, being influenced by systematic effects such as deviations from the assumed flux rise behavior, and possible undetected flux below the survey limits. Thus, while the formal error quantifies the fit precision, the absolute accuracy of the explosion epoch is less certain. This distinction does not affect the broader discussion in this work.

4. Light-curve Properties

4.1. Light Curves and Color Curves

Figure 2 presents the evolution of the light curve for SN 2024pxl in the *uBgVrRiIz* and clear bands, with dense sampling around maximum brightness in all bands. We use a low-order polynomial fit to estimate the time and magnitude at maximum light in the *uBgVrRiIz* bands. Additionally, we estimate the decline in magnitude from the light-curve peak to 15 days after (Δm_{15}) for these bands. These light-curve parameters for SN 2024pxl are listed in Table 1. Figure 3 displays the evolution of SN 2024pxl in the Swift UVOT bands. All bands shown in Figure 3, except for *UVW2* and *UVM2*, cover the peak well. We estimate the Swift UVOT light-curve data parameters in Table 2.

To further explore the nature of the light-curve evolution of SN 2024pxl, we compare its *BgVri* light curves with those of several well-studied SNe Iax (Figure 4). For this, we choose high-luminosity SNe Iax 2002cx (W. Li et al. 2003), 2005hk (M. M. Phillips et al. 2007; D. K. Sahu et al. 2008), 2011ay (T. Szalai et al. 2015), 2012Z (M. D. Stritzinger et al. 2015), 2020rea (M. Singh et al. 2022), and 2020udy (M. Singh et al. 2024); intermediate-luminosity SNe Iax, SN 2019muj (B. Barna et al. 2021); and low-luminosity SNe Iax 2008ha (R. J. Foley et al. 2009), 2010ae (M. D. Stritzinger et al. 2014), and 2019gsc (S. Srivastav et al. 2020; L. Tomasella et al. 2020). These comparison SNe cover both ends of the luminosity distribution for SNe Iax. The rest-frame

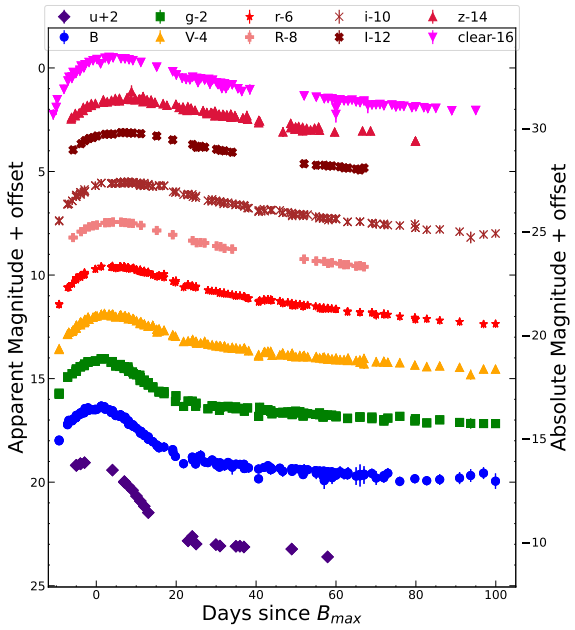

Figure 2. Light-curve evolution of SN 2024pxl in *uBgVrRiIz* and clear bands. Corresponding absolute magnitudes corrected for extinction are also presented on the right-hand ordinate axis. The data behind this Figure is available in machine-readable format. This includes data from Swope, DLT40, KAIT, DECam, LCO, Nickel, Konkoly, and Baja facilities.

(The data used to create this figure are available in the online article.)

magnitudes for each SN displayed in Figure 4 are normalized to the peak in the respective bands.

In the optical bands, SN 2024pxl consistently exhibits decline rates that are faster than those of the high-luminosity SNe Iax and slower than those of the low-luminosity events, placing it between these two groups in terms of photometric evolution. Its behavior is broadly similar to that of the intermediate-luminosity SN 2019muj, although SN 2024pxl evolves somewhat more slowly in several filters. This suggests that SN 2024pxl lies between SN 2019muj and high-luminosity SNe Iax in optical decline rates.

In the UV, SN 2024pxl displays a slow decline relative to other SNe Iax, with a rate comparable to that of a normal SNe Ia (P. A. Milne et al. 2010). This distinguishes its UV behavior from the luminosity-dependent trend observed in the optical bands. A comparison with Swift *UVW1* light curves of SNe 2005hk, 2011ay, 2012Z, 2019muj, 2020kyg, and 2020udy is presented in Figure 5.

Figure 6 illustrates the evolution of SN 2024pxl's colors ($B-V$, $V-I$, $V-R$, and $R-I$) in comparison with other SNe Iax. All colors have been adjusted for total reddening. The color evolution of SN 2024pxl closely resembles that observed in other SNe Iax selected for comparison.

4.2. Bolometric Light Curve

The integrated SED light curve of SN 2024pxl is generated from the *BgVriz* photometry using `SuperBol` (M. Nicholl 2018), incorporating the distance and extinction values outlined in Section 3. `SuperBol` takes the dereddened fluxes and uncertainties across passbands to construct an SED at each epoch. Luminosities are determined by integrating this spectrum while propagating uncertainties. To account for missing passbands in the UV and NIR, `SuperBol` fits a

Table 1
Light-Curve Parameters of SN 2024pxl

SN 2024pxl	u band	B band	g-band	V band	r band	R band	i band	I band	z band
JD of maximum light (2,460,000+)	523.00 ± 0.5	524.6 ± 0.5	525.2 ± 0.5	527.4 ± 0.5	528.14 ± 0.5	529.4 ± 0.5	530.2 ± 0.5	531.1 ± 0.5	531.7 ± 0.5
Magnitude at maximum (mag)	17.02 ± 0.01	16.42 ± 0.02	16.10 ± 0.01	15.90 ± 0.01	15.56 ± 0.01	15.44 ± 0.01	15.49 ± 0.01	15.12 ± 0.02	15.47 ± 0.07
Absolute magnitude at maximum (mag)	−15.87 ± 0.19	−16.30 ± 0.19	−16.60 ± 0.19	−16.81 ± 0.19	−17.13 ± 0.19	−17.45 ± 0.19	−17.22 ± 0.19	−17.77 ± 0.19	−17.24 ± 0.21
Δm_{15} (mag)	2.54 ± 0.05	1.80 ± 0.07	1.56 ± 0.04	0.87 ± 0.06	0.49 ± 0.05	0.66 ± 0.03	0.51 ± 0.02	0.40 ± 0.04	0.46 ± 0.08

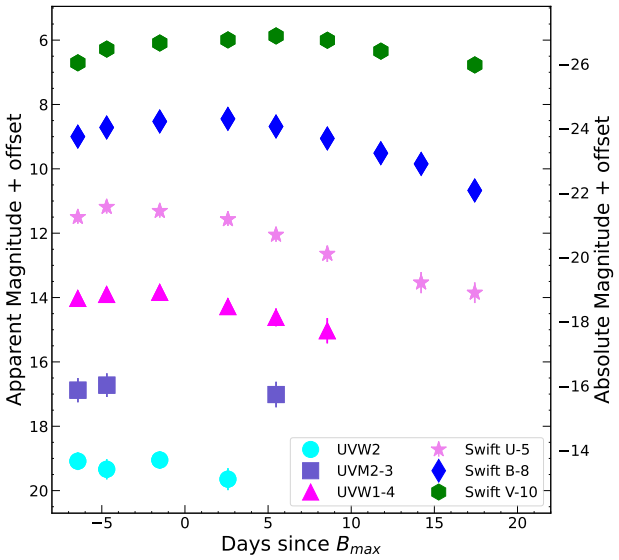

Figure 3. Light-curve evolution of SN 2024pxl in the Swift bands.

blackbody to each SED to derive a correction that is then applied to the integrated SED luminosities.

The integrated SED light curves of the other comparison SNe presented in Figure 7 are constructed using a similar approach. SN 2018cni (M. Singh et al. 2023), another high-luminosity SN Iax, is also included for comparison in Figure 7. The peak integrated SED *BgVriz* luminosity of SN 2024pxl is $(7.82 \pm 0.36) \times 10^{41}$ erg s^{-1}. SN 2024pxl is less luminous than all the high-luminosity SNe Iax, such as SNe 2012Z, 2020rea, and 2020udy, but is brighter than the intermediate-luminosity SNe Iax, SN 2019muj. SN 2024pxl lies in the gap between the high-luminosity and low-luminosity SNe Iax, in agreement with our decline rate comparison (Section 4.1).

We conduct analytical modeling of the integrated SED light curve for SN 2024pxl using the methods outlined by W. D. Arnett (1982) and S. Valenti et al. (2008). The basic assumptions of this model consist of a small initial radius, constant optical opacity, spherically symmetric and optically thick ejecta, and the inclusion of ^{56}Ni in the ejected material. By fitting the integrated SED light curve of SN 2024pxl, we estimate a ^{56}Ni mass of $0.027 \pm 0.002\,M_{\odot}$, an ejecta mass of $0.36 \pm 0.05\,M_{\odot}$, and a rise time of 11 days, with uncertainties derived from the covariance matrix. We note that this small formal error represents only the statistical uncertainty from the fit and does not capture systematic effects arising from model assumptions. The true uncertainty is expected to be larger, and the value should be regarded as a model-dependent estimate.

For the fit, we assume a constant opacity of $\kappa_{\rm opt} = 0.1$ cm^2 g^{-1} and a photospheric velocity of 5000 km s^{-1} at maximum brightness. Directly estimating the photospheric expansion velocity from the bottom panel of Figure 8, we calculate $dR_{\rm BB}/dt \approx 10{,}000$ km s^{-1} over the nearly linear expansion period from maximum light to +15 days. It is surprising that this value is larger than the typical photospheric absorption-line velocities, perhaps suggesting that the optical depth approaches unity farther out in the ejecta than the lines would predict.

We also compared the evolution of the blackbody temperature and radius of SN 2024pxl with those of other SNe Iax (Figure 8). The blackbody temperature of SN 2024pxl is lower than that of the different comparison SNe before maximum light. After that, it remains at the lower end of the blackbody temperature distribution. It is possible that this could be the effect of underestimated extinction. The evolution of the blackbody radius of SN 2024pxl is proportional to the luminosity of the SN, which is positioned in an intermediate location in Figure 8. SN 2024pxl's blackbody temperature and radius evolution align well with the characteristic patterns seen in other SNe Iax.

For SNe Iax, contributions from the unobserved UV and IR passbands remain poorly constrained. However, based on available data for a few SNe Iax, the combined UV and NIR contributions to the total bolometric flux have been estimated. M. M. Phillips et al. (2007) demonstrated that the UV flux accounts for approximately 20% of the UV-through-IR light curve for an early photospheric phase in the case of SN 2005hk. Similarly, M. Yamanaka et al. (2015) estimated that the NIR band makes up about 20% of the optical+NIR flux around peak light for SN 2012Z. L. Tomasella et al. (2016) found that the UV+IR flux collectively accounted for ∼35% of the total emission in SN 2014ck. Moreover, S. Srivastav et al. (2020) and A. Dutta et al. (2022) calculated the ratio of $L_{\rm peak,pseudo}$ (peak integrated SED luminosity) to $L_{\rm peak,bb}$ (peak blackbody luminosity) as 0.69 for SN 2019gsc and 0.62 for SN 2020sck, respectively. In the case of SN 2020kyg, S. Srivastav et al. (2022) reported that about 60% of the total bolometric luminosity near-maximum light is attributed to the optical emission.

We have Swift observations that capture the light-curve evolution of SN 2024pxl around the peak. Using `SuperBol` for *UVW2*, *UVM2*, *UVW1*, and *U* filters along with *BgVriz* filters, we find that the ratio of peak integrated SED luminosity using *BgVriz* and *SDAUBgVriz* bands ($S = UVW2$, $D = UVM2$, $A = UVW1$, Swift $U = U$) is ∼0.75, suggesting that the UV may be contributing up to ∼25% of the bolometric luminosity near peak. Using the same analytical model for the *SDAUBgVriz* integrated SED light curve, we find that $\sim 0.03 \pm 0.01\,M_{\odot}$ of ^{56}Ni is synthesized during the explosion of SN 2024pxl. While this result is consistent with our earlier optical-only ^{56}Ni mass estimate ($0.026 \pm 0.002\,M_{\odot}$), the quoted uncertainties represent formal errors from the fitting procedure and do not fully capture systematic effects associated with the simplifying assumptions of the analytic model (e.g., constant opacity, spherical symmetry).

M. Fink et al. (2014) presented numerical calculations for deflagration models of CO WDs with varying explosion energy (parametrized by the number of ignition kernels). These models span a broad range of explosion parameters (^{56}Ni mass 0.03–0.38 $M_{\odot}$, rise time 7.6–14.4 days). The estimated mass of ^{56}Ni ($0.03\,M_{\odot}$) and rise time (11 days) for SN 2024pxl are consistent with the range provided by these models. However, the peak magnitude in the *V* band for SN 2024pxl ($M_V = -16.81 \pm 0.19$ mag) is on the fainter end of the estimation (−16.84 to −18.96 mag) given by M. Fink et al. (2014). The mass of ^{56}Ni in the case of SN 2024pxl matches the ^{56}Ni synthesized in the weakest-energy N1def (single ignition point) model presented by M. Fink et al. (2014). Radiative-transfer modeling based on the N1def model by L. A. Kwok et al. (2025) shows good agreement with the spectra of SN 2024pxl from the optical through the MIR.

For low-luminosity SNe Iax, M. Kromer et al. (2015) studied the deflagration of a hybrid CONe WD. Our estimated peak magnitude of SN 2024pxl in the *B* band

Table 2
Light-Curve Parameters of SN 2024pxl for Swift Data

SN 2024pxl	*UVW2*	*UVM2*	*UVW1*	Swift *U*	Swift *B*	Swift *V*
JD of maximum light (2,460,000+)	⋯	⋯	521.5 ± 0.5	521.9 ± 0.5	525.3 ± 0.5	527.8 ± 0.5
Magnitude at maximum (mag)	⋯	⋯	17.83 ± 0.14	16.21 ± 0.08	16.46 ± 0.06	15.90 ± 0.07
Absolute magnitude at maximum (mag)	⋯	⋯	−14.91 ± 0.24	−16.53 ± 0.20	−16.28 ± 0.20	−16.84 ± 0.20
Δm_{15} (mag)	⋯	⋯	1.46 ± 0.61	2.17 ± 0.32	1.78 ± 0.15	0.95 ± 0.12

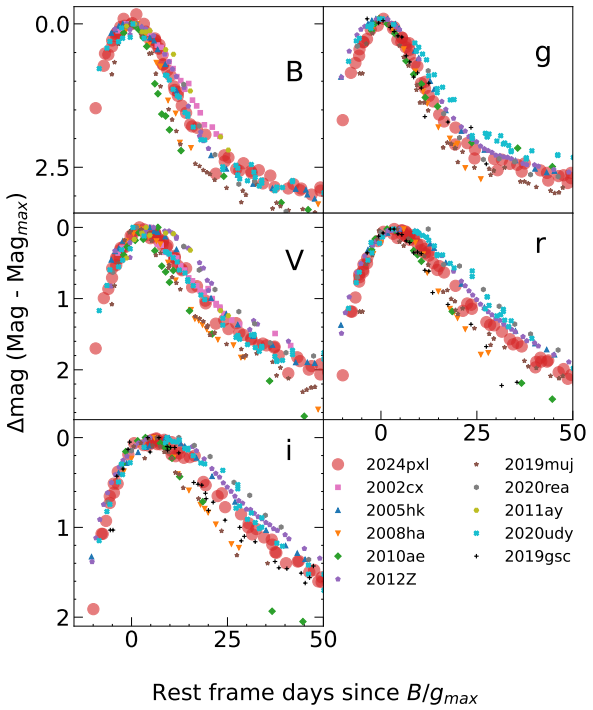

Figure 4. Comparison of the light-curve evolution of SN 2024pxl in *BgVri* bands with other well-studied SNe Iax. The *B*-band maximum date serves as the reference for comparison plots in both *B* and *V* bands, while *gri*-band comparison plots are referenced to *g*-band maximum brightness.

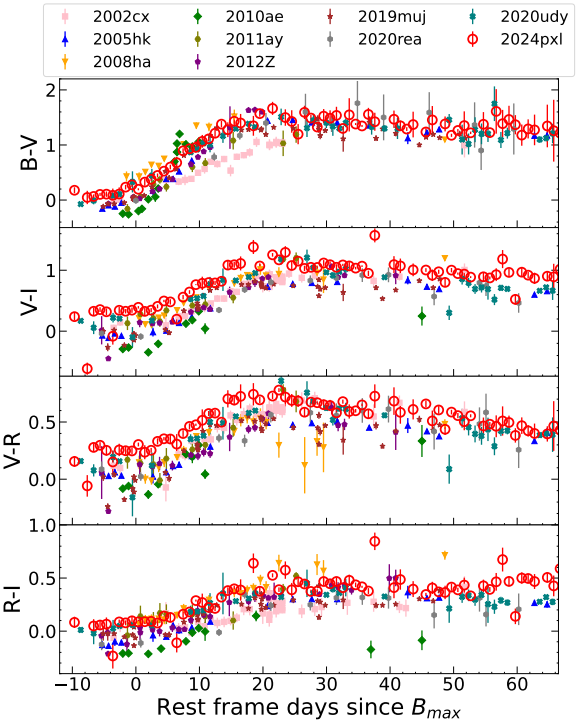

Figure 6. Comparison of the color (mag) evolution of SN 2024pxl with other well-studied SNe Iax.

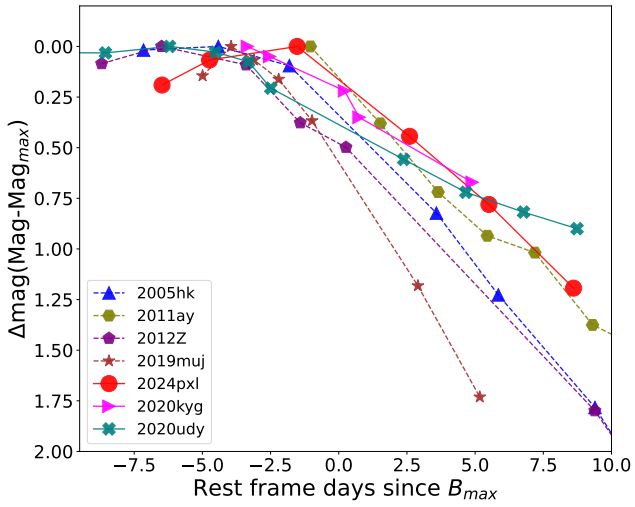

Figure 5. Comparison of the light-curve evolution of SN 2024pxl in the Swift *UVW1* band with other SNe Iax.

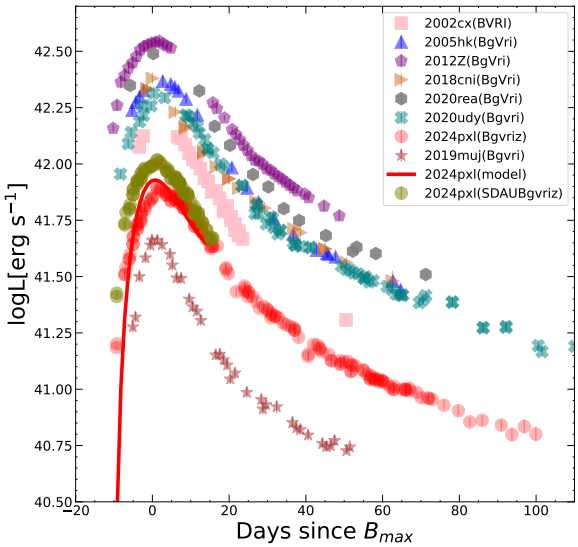

Figure 7. Comparison of *BgVriz* integrated SED light curve of SN 2024pxl (red circles) with other well-studied SNe Iax. The solid red line presents the analytical model fit to the integrated SED light curve of SN 2024pxl. We also plot the integrated SED light curve of SN 2024pxl using data in UV bands (olive circles), which lies slightly above the *BgVriz* integrated SED light curve.

(−16.30 ± 0.19 mag) and mass of ^{56}Ni (0.03 $M_\odot$) exceed the predictions from the hybrid CONe WD model (B_{max} = −13.2 to −14.6 mag, mass of ^{56}Ni =3.4 × 10^{-3} $M_\odot$) that may apply to lower-luminosity objects. These results also favor the

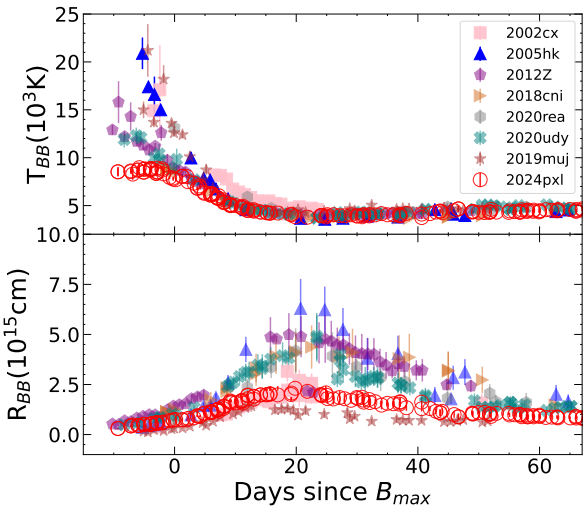

Figure 8. Evolution of the blackbody temperature and radius of SN 2024pxl (red circles), along with other SNe Iax used for comparison.

interpretation that SN 2024pxl is an interesting luminosity link, with explosion parameters higher than those predicted for low-luminosity objects but lying at the lower end of the models proposed to explain the high-luminosity members of the class.

5. Spectral Evolution

5.1. Spectral Features and Comparisons

Figures 9, 10, and 11 present the spectral evolution (Table 4) of SN 2024pxl from approximately −9 to +89 days relative to B_{max}. Spectra were obtained nearly daily for almost 2 months after maximum, producing a rich dataset allowing detailed tracking of spectral evolution. We compare the spectral features of SN 2024pxl with those of other well-studied SNe Iax at similar premaximum, near-maximum, postmaximum, and late phases in Figures 12, 13, 14, and 15, respectively.

5.1.1. Premaximum Spectra

We observe that at early, prepeak times, SN 2024pxl has a flat continuum consistent with the low temperatures we infer from the photometry (see Figure 8). The early-time spectra of SN 2024pxl display features such as Fe III, Fe II, and Si II (Figure 12). In agreement with our findings that SN 2024pxl is a photometrically intermediate SNe Iax, it is spectroscopically intermediate as well, sharing similarities with both high-luminosity SNe Iax (e.g., SNe 2012Z, 2005hk, and 2020udy) and low-luminosity objects (e.g., SNe 2010ae and 2008ha). Specifically, SN 2024pxl has weak Si II features but also exhibits a C II line at 6580 Å. In high-luminosity SNe Iax, the Si II line is relatively weak, and C II is generally not detected. In contrast, in low-luminosity SNe Iax, these features are much more prominent. The Ca II NIR triplet is present in SN 2024pxl but is weaker than in SNe 2010ae and 2008ha. This combination of weak Si II and the presence of C II suggests that SN 2024pxl also serves as a spectroscopic transitional link between high-luminosity and low-luminosity SNe Iax.

5.1.2. Near-maximum Spectra

The peak brightness spectrum of SN 2024pxl (Figure 13) shows an increase in the strength of the Si II line at 6355 Å and the Fe III feature near 4400 Å. At this epoch, SN 2024pxl resembles SNe 2019muj (intermediate luminosity) and 2020rea (high luminosity). The Fe II features near 5000 Å are similar to those in SNe 2002cx, 2005hk (both high luminosity), and 2019muj, while features near 4000 Å match well with those of SN 2020rea. We detect the Ca II NIR triplet in SN 2024pxl, which is not detected in high-luminosity objects, but is even more pronounced in the low-luminosity SN 2010ae. The combination of Ca II NIR features similar to low/intermediate-luminosity objects, and Fe II characteristics shared with more luminous SNe Iax again implies that SN 2024pxl represents a transitional case.

5.1.3. Postmaximum and Late-time Spectra

Figure 14 shows the postmaximum spectra of SN 2024pxl in the context of other objects. At these epochs, SN 2024pxl closely resembles SN 2019muj, an intermediate-luminosity SNe Iax. During the postmaximum phase, the Si II and C II lines vanish, giving way to Fe and Co lines in the 5000–7000 Å range. Iron-group elements (IGEs) and a strong Ca II NIR triplet dominate the postmaximum spectra, similar to other high- and intermediate-luminosity objects. Low-luminosity SNe Iax (e.g., SNe 2010ae and 2008ha, shown in Figure 14) evolve more rapidly and exhibit narrower spectral signatures than SN 2024pxl. The Cr II feature near 4800 Å and the Co II lines near 6500 Å in SN 2024pxl share resemblance with high-luminosity SNe 2002cx and 2019muj. Additionally, the Ca II NIR triplet in SN 2019muj is strikingly similar to that in SN 2024pxl.

We compare the late-time spectrum of SN 2024pxl obtained at ∼+89 days with spectra of SNe 2008ge (R. J. Foley et al. 2010), 2014dt (M. Singh et al. 2018), and 2020udy at similar epochs (Figure 15). At late times, the spectral lines become narrower, and several forbidden emission lines such as [Fe II], [Ni II], and [Ca II] emerge along with narrow permitted lines such as Fe II. The strength of these forbidden lines increases with the cooling of the ejecta (R. J. Foley et al. 2016). Owing to their intrinsically low luminosity, late-time spectra of SNe Iax are rare. The late-time spectra of SNe Iax vary widely, with some showing broad emission lines and others dominated by narrow features (R. J. Foley et al. 2016). Of the comparison SNe in Figure 15, SN 2024pxl most closely resembles SN 2014dt, exhibiting narrower lines than the higher-luminosity objects SNe 2020udy and 2008ge. The narrow features seen in the late-phase spectra of SNe Iax are thought to originate from the innermost regions (K. Maeda & M. Kawabata 2022; Y. Camacho-Neves et al. 2023). Additional late-time observations of SNe Iax across the luminosity distribution will help to understand the origin and nature of these spectral features more precisely.

Overall, at postmaximum and late times, SN 2024pxl shares similarities with high-luminosity SNe Iax and intermediate-luminosity SNe Iax, SN 2019muj.

5.1.4. NIR Spectra

Figure 16 displays the NIR spectral evolution of SN 2024pxl from −6.7 to +42.5 days post B maximum. The first two NIR spectra of SN 2024pxl show underdeveloped Fe II features with evidence for the Mg II λ10,952 line. Possible signatures of C I λ10,693 and C I λ11,754 are suggested in the early NIR spectra of SN 2024pxl. As the ejecta cool and expand, the spectrum-formation region recedes to lower velocities, and

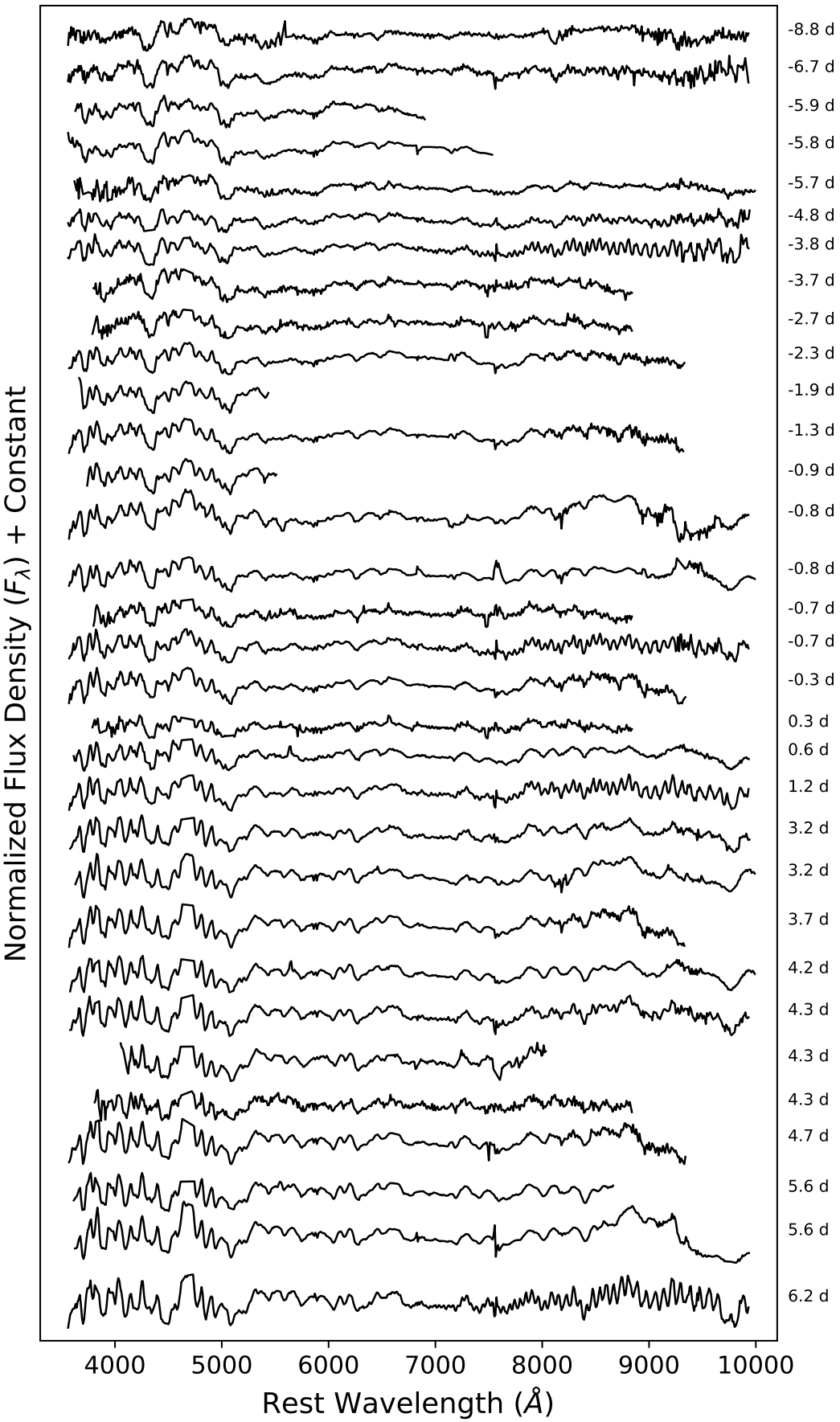

Figure 9. Spectral evolution of SN 2024pxl spanning from −8.8 to 5.6 days after *B*-band maximum brightness. The 91 optical spectra shown in Figures 9–11 are available in machine-readable format in a .tar.gz package.

(The data used to create this figure are available in the online article.)

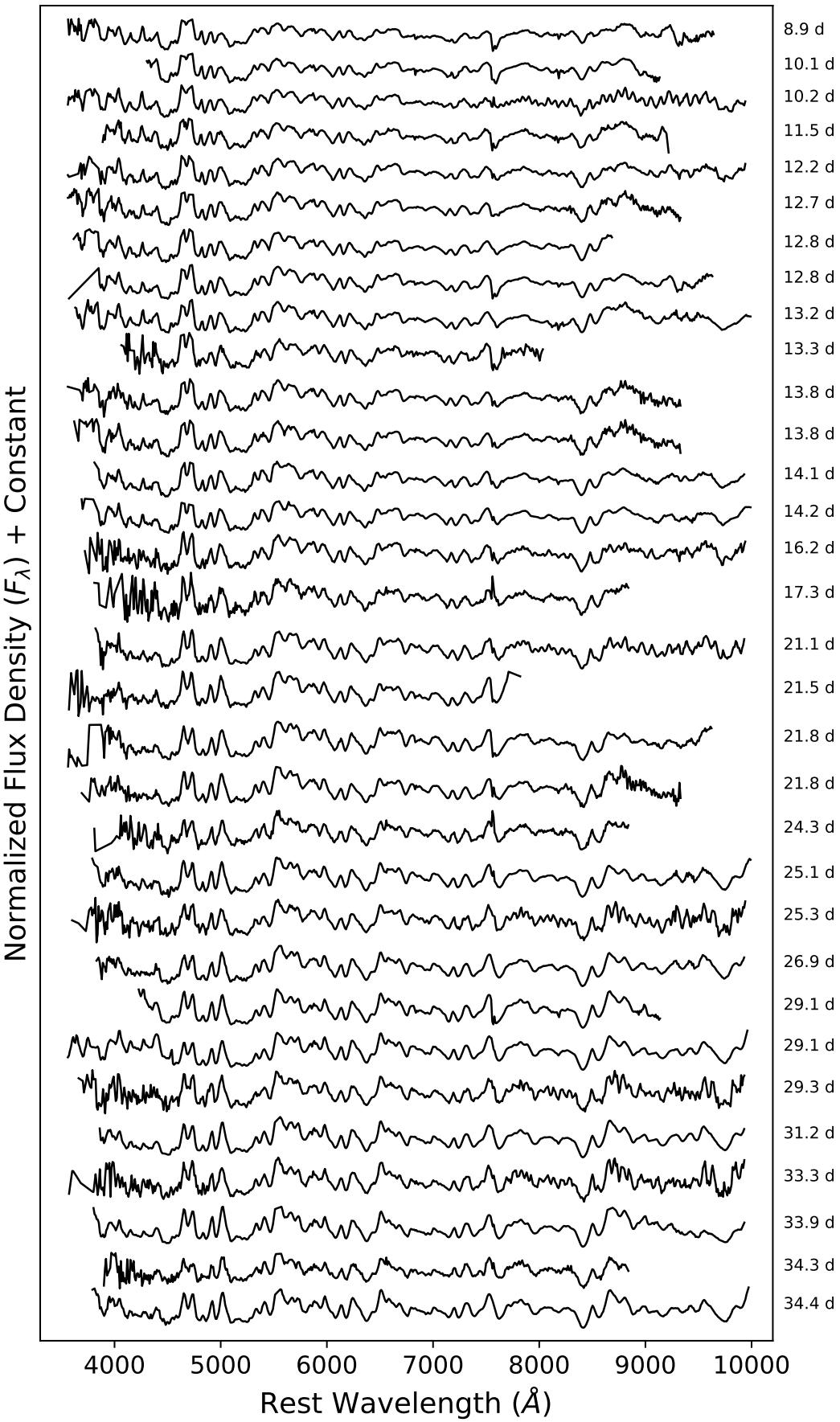

Figure 10. Spectral evolution of SN 2024pxl spanning from 6.2 to 34.3 days after *B*-band maximum brightness.

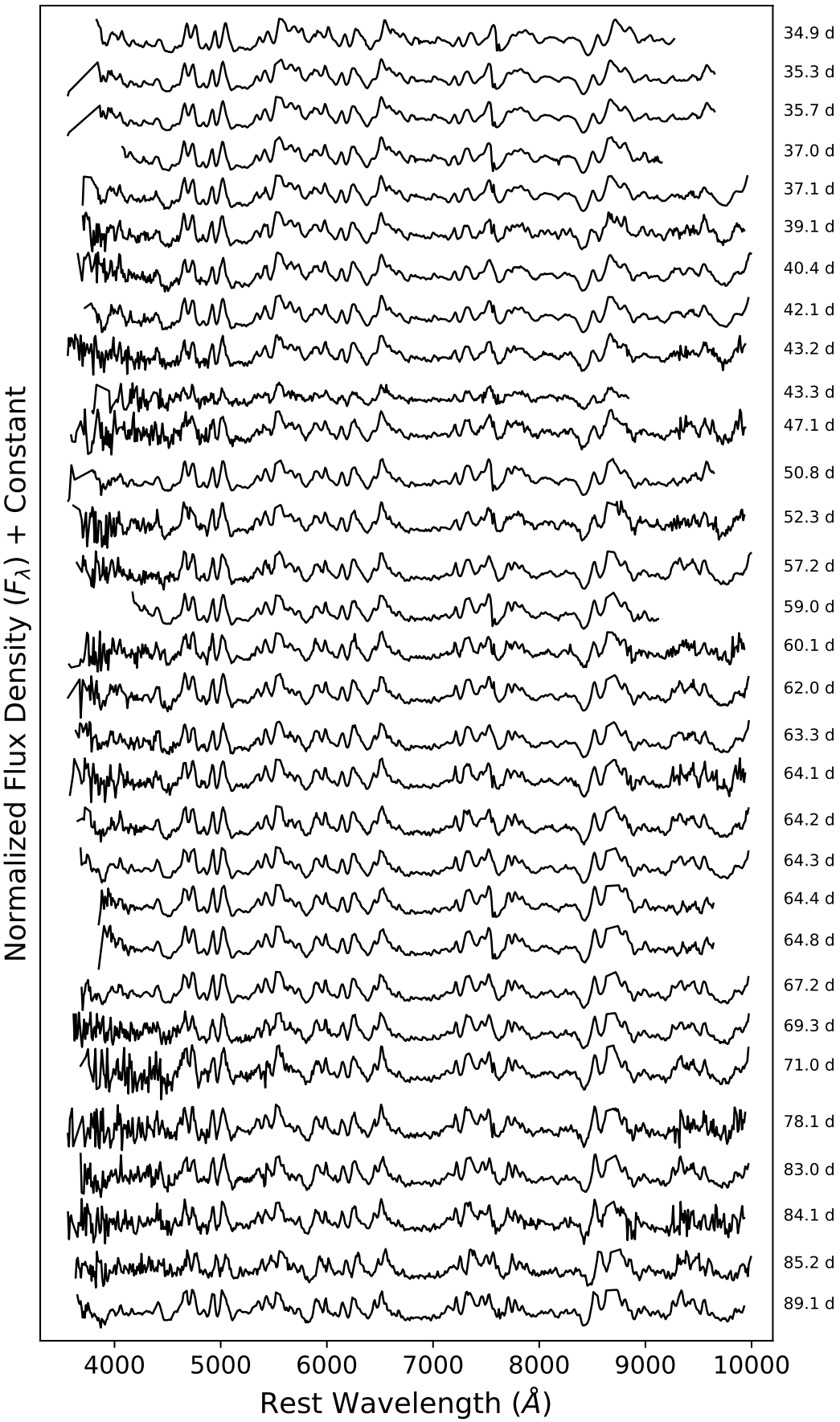

Figure 11. Spectral evolution of SN 2024pxl spanning from 34.4 to 89.1 days after *B*-band maximum brightness.

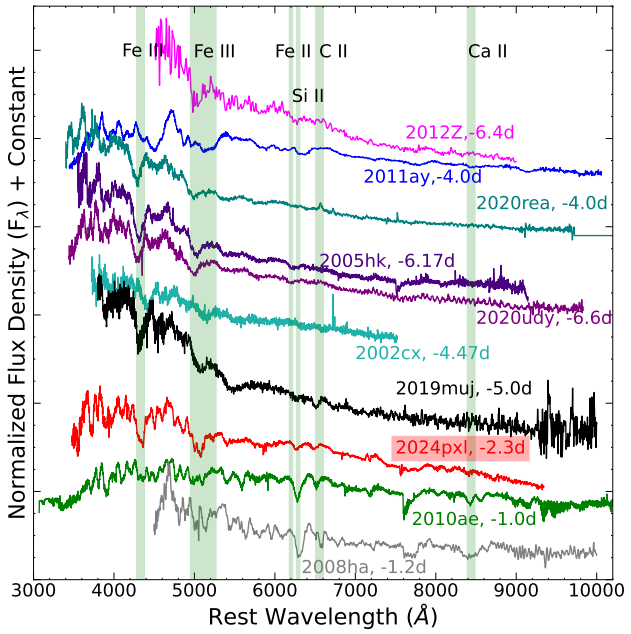

Figure 12. Prepeak spectral comparison of SN 2024pxl (red) with other SNe Iax at similar epochs.

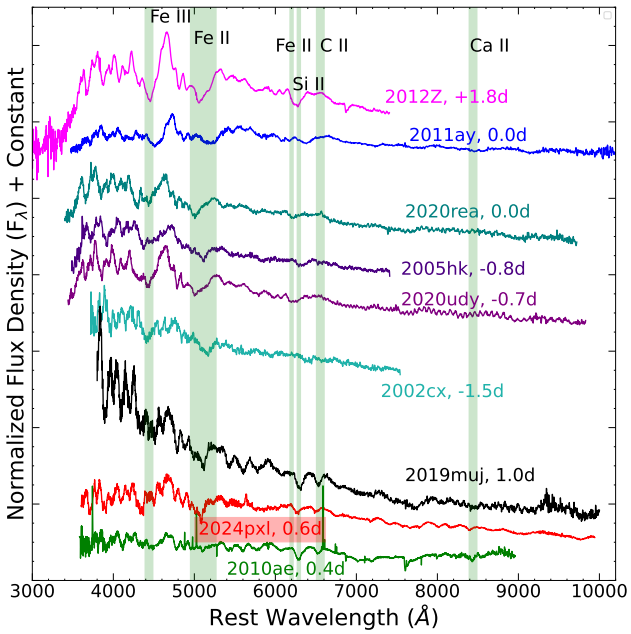

Figure 13. Near-maximum-light spectral comparison of SN 2024pxl (red) with other SNe Iax at similar epochs.

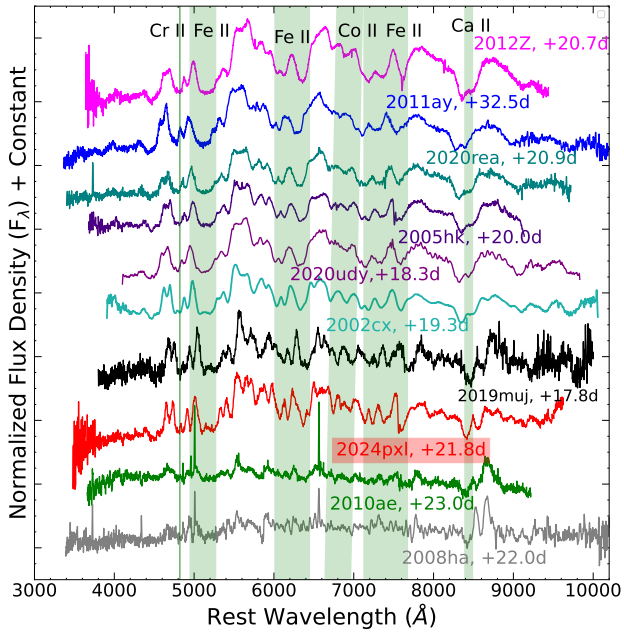

Figure 14. Postmaximum spectral comparison of SN 2024pxl (red) with other SNe Iax at similar epochs.

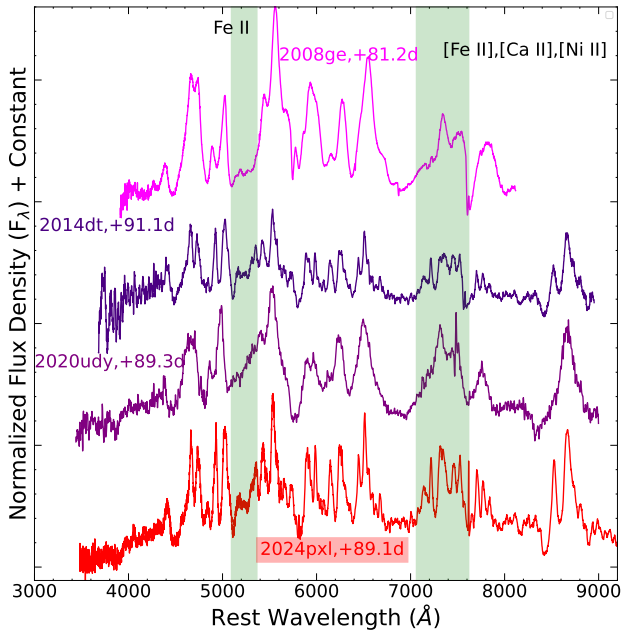

Figure 15. Late-time spectral comparison of SN 2024pxl (red) with other SNe Iax at similar epochs. We highlight a few nebular features in green.

lines become somewhat less blended, with the Co II lines increasing in prominence over time. Our spectral sequence shows that Fe II and Co II lines dominate the NIR. These lines are distinctive features in the NIR spectra of all SNe Iax (M. D. Stritzinger et al. 2014), and Figure 17 displays this similarity in NIR spectra from bright to faint objects.

The NIR spectrum of SN 2024pxl at +23.4 days shows more similarities to the high-luminosity SN 2005hk (M. Kromer et al. 2013) than with the intermediate-luminosity SN 2019muj (B. Barna et al. 2021) and low-luminosity SN 2010ae (M. D. Stritzinger et al. 2014). In particular, the Mg II absorption, the features at 12,000 and 12,700 Å, and the prominence of the Co II lines in the 16,000 Å region are differentiating features. Where SN 2024pxl resembles SN 2005hk, SN 2019muj instead resembles SN 2010ae, mainly owing to the lower velocities that allow individual lines to be separated more clearly. This NIR spectral comparison provides additional support that intermediate-luminosity objects of the class (like SNe 2024pxl and 2019muj) are transitional between high- and low-luminosity objects.

5.2. Velocity Evolution

We probe the evolution of velocities of C II, Si II, and Fe II lines using our optical spectral sequence, and the Co II lines from our NIR spectra. We measure line velocities by

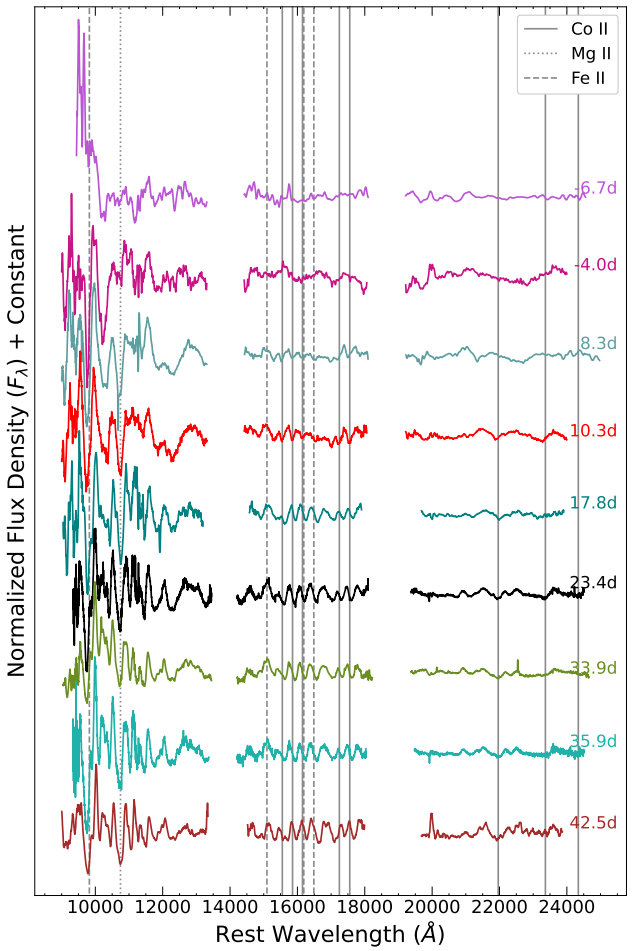

Figure 16. NIR spectroscopic evolution of SN 2024pxl. The 9 NIR spectra shown in this Figure are available in machine-readable format in a .tar.gz package.

(The data used to create this figure are available in the online article.)

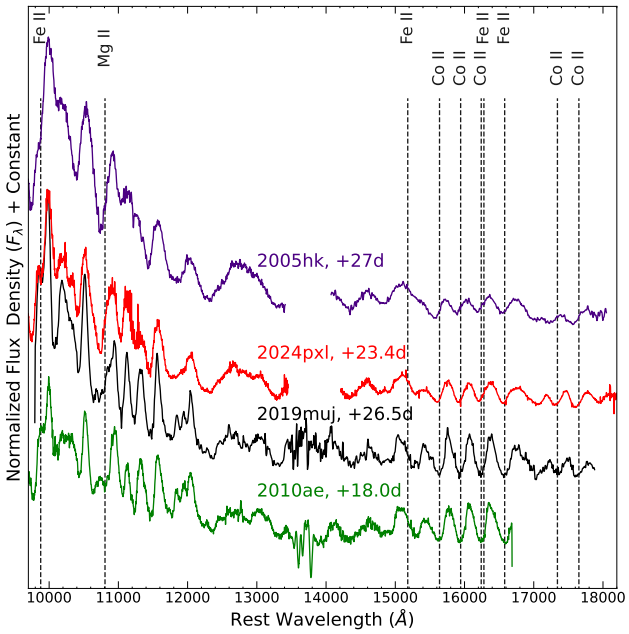

Figure 17. Comparison of the NIR spectral features of SN 2024pxl with high-luminosity SNe Iax, SN 2005hk, low-luminosity SNe Iax, SN 2010ae, and intermediate-luminosity SNe Iax, SN 2019muj.

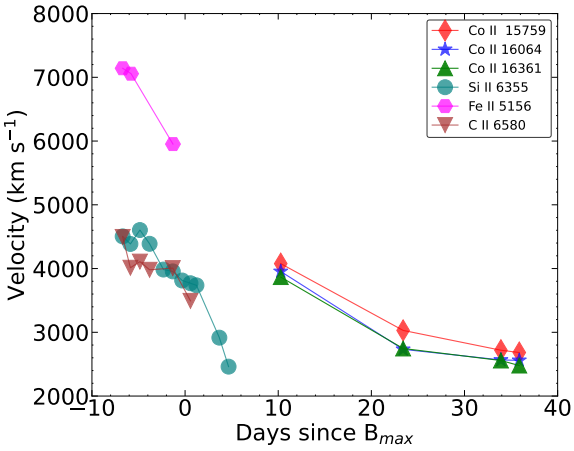

Figure 18. Evolution of the line velocities of Si II, C II, Fe II, and Co II lines in SN 2024pxl.

fitting Gaussian profiles to the absorption trough of the P Cygni profiles of the C II λ6580, Si II λ6355, Fe II λ5156, Co II λ15,759, Co II λ16,064, and Co II λ16,361 lines (Figure 18). This standard method of measuring photospheric line velocities results in Co II measurements that are consistent with those presented by L. A. Kwok et al. (2025), obtained by fitting blended Co II lines simultaneously. Figure 19 shows the Si II line-velocity evolution for SN 2024pxl alongside several other well-studied SNe Iax. The uncertainties presented in Figure 19 could likely be underestimated, as we only account for measurement uncertainties from our fitting (and not for the effects of line blending, for example).

SN 2024pxl exhibits lower velocities than other SNe shown in Figure 19, except low-luminosity SN 2008ha. The prominent Si II line is overlapped by a continuously growing Fe II feature in the red wing of the Si II line. As a result, we systematically underestimate the velocities associated with this line over time by considering it as a single absorption feature. In the case of high-luminosity SN 2020udy, K. Maguire et al. (2023) showed that the Si II line is contaminated by the Fe II line before maximum light, although Si II is present in postmaximum spectra. This might be why a significant drop is observed in the Si II velocities postmaximum in SN 2024pxl. It is likely that more careful modeling of these lines will be required to obtain a more accurate comparison of the Si II line-velocity evolution across SNe Iax.

The Si II and C II line velocities of SN 2024pxl at peak are 3800 and 3500 km s^{-1}, respectively. The measured Fe II velocities are 7100, 7060, and 5950 km s^{-1} at epochs ~ -6.7, -5.8, and -1.3 days since $B_{\rm max}$, respectively. At a similar epoch, the estimated velocities using Fe II lines are higher than the Si II and C II line velocities, indicating significant mixing in the burning products (M. M. Phillips et al. 2007). L. A. Kwok et al. (2025) also find evidence of mixing in SN 2024pxl from the emission lines of IGEs and intermediate-mass elements (IMEs), which are all centrally peaked and have similar velocity offsets and widths. The measured Co II line velocities in the NIR region for SN 2024pxl at an epoch of 23.4 days are 3030, 2730, and 2750 km s^{-1} for Co II λ15,759, Co II λ16,064, and Co II λ16,361, respectively (consistent with one another), and slightly higher than those reported by B. Barna et al. (2021) at

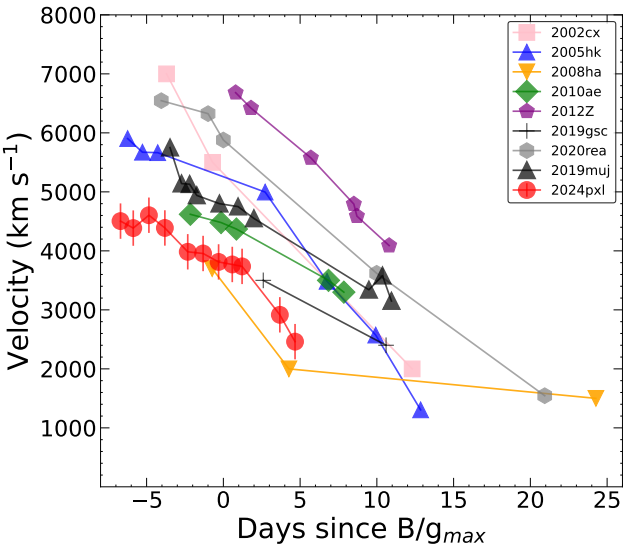

Figure 19. Evolution of the velocity at maximum absorption of Si II λ6355 for SN 2024pxl and its comparison with other SNe Iax.

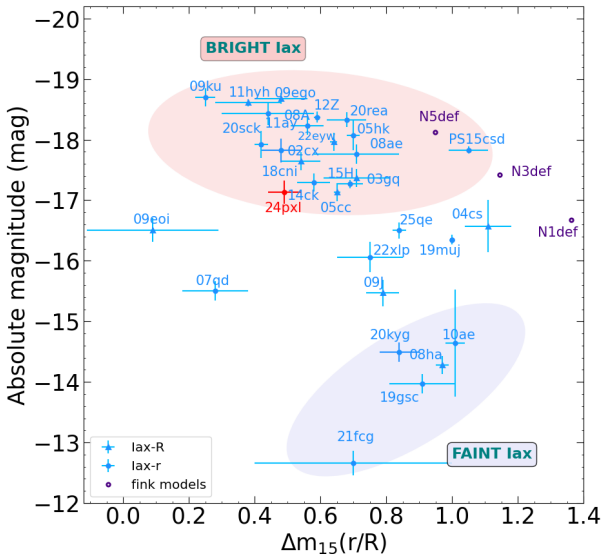

Figure 20. This figure illustrates the distribution of SNe Iax in the absolute magnitude–light-curve decline rate plane in the r /R bands. SN 2024pxl is marked by a red-filled circle.

an epoch of 26.5 days past $B_{\max}$ for intermediate-luminosity SN 2019muj. At a comparable epoch, velocities of Co II lines in low-luminosity SN 2010ae (M. D. Stritzinger et al. 2014) are lower than in SN 2024pxl.

6. Summary

SN 2024pxl is a nearby SNe Iax with an early detection that enabled precise constraints on its rise time. With a peak absolute magnitude of $M_{V,\max} = -16.81 \pm 0.19$ mag, SN 2024pxl is an intermediate-luminosity SNe Iax similar to SN 2019muj. The color evolution of SN 2024pxl aligns closely with that of other SNe Iax. Utilizing Swift UV coverage around peak brightness, we estimate the contribution of UV flux to the bolometric luminosity and find that SN 2024pxl's pseudo-bolometric luminosity falls between those of SNe 2002cx and 2019muj, placing it in a unique intermediate position in the luminosity range of SNe Iax. Analytical modeling of the integrated SED light curve indicates the synthesis of $0.03 \pm 0.01\,M_{\odot}$ of ^{56}Ni and an ejected mass of $0.36 \pm 0.05\,M_{\odot}$. The explosion parameters calculated through analytical modeling of the integrated SED light curve are consistent with the N1def model from M. Fink et al. (2014), a weak deflagration of a near-$M_{\rm Ch}$ WD with one ignition point. This is consistent with the results of L. A. Kwok et al. (2025) that SN 2024pxl displays spectroscopic similarity to the predictions of the N1def model.

Our spectral comparisons also suggest that SN 2024pxl is a transitional object between high-luminosity and low-luminosity SNe Iax. It exhibits many similarities to intermediate-luminosity SN 2019muj and high-luminosity SNe Iax. In the early spectral sequence, we also detect C II that is seen more prominently in less luminous objects. Additionally, the late-time spectra of SN 2024pxl show narrow emission lines around 7300 Å whereas the high-luminosity objects (e.g., SNe 2008ge and 2020udy) display broader features.

In the NIR, SN 2024pxl shows signatures from Mg II, Fe II, and Co II, and it resembles the high-luminosity SNe Iax, SN 2005hk, while intermediate-luminosity SNe Iax, SN 2019muj, more closely resemble the low-luminosity SNe Iax, SN 2010ae. This is mainly due to more line blending in SN 2024pxl compared with SN 2019muj, caused by wider line widths. Despite the higher velocities indicated by the wider line widths in SN 2024pxl, the evolution of the photospheric velocity of SN 2024pxl shows systematically lower velocities relative to other comparison SNe, except for the very low-luminosity SN 2008ha. L. A. Kwok et al. (2025) find potential evidence for bulk motion on the order of a few hundred kilometers per second in the ejecta of SN 2024pxl from measurements of MIR forbidden lines, which would impact the true versus observed photospheric velocity. Given the spectroscopically and photometrically intermediate position of SN 2024pxl between SN 2019muj and brighter SNe Iax, we suggest that velocity measurements of the widths of the Co II lines may be better correlated with luminosity than the photospheric velocity. These spectral properties provide evidence that SN 2024pxl is a transitional SNe Iax.

We measure the Fe II velocity to be substantially higher than that of Si II and C II at similar epochs. At a slightly later phase, Co II velocity measurements seem to align with the expected velocity decay from the Fe II measurements. Higher velocities of IGEs compared to IMEs indicate mixing in the ejecta, consistent with the findings of L. A. Kwok et al. (2025).

Figure 20 shows the distribution of SNe Iax in terms of their peak absolute magnitude and light-curve decline rate in the r/R band. The data are taken from M. Singh et al. (2023) and references therein, augmented with the recently studied SNe Iax events SN 2022eyw (H. Das et al. 2025), SN 2022xlp (D. Bánhidi et al. 2025), SN 2025qe (M. R. Magee et al. 2025), and SN 2024pxl. M. Singh et al. (2023) suggested that bright (high-luminosity) SNe Iax have $M_r \leqslant -17.1$ mag, while faint (low-luminosity) ones have $M_r \geqslant -14.64$ mag, and further proposed a negative linear correlation for the bright population and a positive correlation for the faint population. SN 2024pxl lies near the faint boundary of the bright SNe Iax group, whereas SN 2022eyw is a luminous member located well within the bright population. In contrast, SNe 2022xlp and 2025qe exhibit intermediate luminosities, bridging the bright and faint subclasses. The newly added events follow the overall trend, with SN 2024pxl positioned close to the lower

end of the bright group, underscoring its transitional nature. As additional SNe Iax spanning the full luminosity range become available, these correlations can be tested more robustly.

Overall, SN 2024pxl is a compelling link between high-luminosity and low-luminosity SNe Iax. The analysis of UV, optical, and NIR data presented in this work, and the spectral analysis of JWST NIR and MIR data by L. A. Kwok et al. (2025), demonstrate that SN 2024pxl is photometrically and spectroscopically consistent with the one-ignition-point weak deflagration model, N1def, from M. Fink et al. (2014). L. A. Kwok et al. (2025) also show that SN 2024pxl shares spectroscopic similarities (aside from the large luminosity difference) with the very faint SNe Iax, SN 2024vjm. These findings indicate that intermediate-luminosity objects such as SNe 2019muj and 2024pxl are links in a continuous distribution. Future studies of other SNe Iax with rich datasets, such as that presented for SN 2024pxl, from both ground- and space-based telescopes will help us better understand the nature of these peculiar SNe.

Remarkably, the diverse class of SNe Iax can span a huge luminosity range. Still, the seemingly continuous properties we observe may yet point to a common (or at least quite similar) progenitor origin and explosion mechanism. This contrasts with normal SNe Ia, for which multiple progenitor pathways may be plausible while producing more homogeneous outcomes. Further study of peculiar thermonuclear SNe holds promise to enable a better understanding of which WDs may explode and their explosion mechanisms.

Acknowledgments

We thank the referee for the careful review and valuable suggestions, which have helped refine the manuscript. We also thank Stéphane Blondin for helpful comments, which improved the manuscript.

This work is based in part on observations collected at the European Southern Observatory under ESO program 114.27JL.001. Partly based on observations made with the Nordic Optical Telescope, owned in collaboration by the University of Turku and Aarhus University. This work also makes use of data gathered with the 6.5 m Magellan telescopes at Las Campanas Observatory, Chile. A FIRE spectrum was obtained through A.P.'s prior support by a Carnegie Fellowship. This work makes use of data from the LCO global network of telescopes. The LCO group is supported by National Science Foundation (NSF) grants AST-1911151 and AST-1911225.

The SALT observations were obtained with Rutgers University program 2024-1-MLT-004 (PI L. A. Kwok). We are grateful to SALT Astronomer Rosalind Skelton for taking these data. Data reported here were obtained in part at the MMT Observatory, a joint facility of the University of Arizona and the Smithsonian Institution. We sincerely thank the MMT observers and staff for their accommodation of our strict timing requirements to ensure they coincided with JWST observations.

Some of the data presented herein were obtained at the W. M. Keck Observatory, which is operated as a scientific partnership among the California Institute of Technology, the University of California, and NASA. The Observatory was made possible by the generous financial support of the W. M. Keck Foundation. This work was supported by a NASA Keck PI Data Award (PI: D. J. Sand), administered by the NASA Exoplanet Science Institute. The authors wish to recognize and acknowledge the very significant cultural role and reverence that the summit of Maunakea has always had within the Indigenous Hawaiian community. We are most fortunate to have the opportunity to conduct observations from this mountain.

This study employs observations obtained with the Hobby–Eberly Telescope (HET), which is a joint project of the University of Texas at Austin, the Pennsylvania State University, Ludwig-Maximilians-Universität München, and Georg-August-Universität Göttingen. The HET is named in honor of its principal benefactors, William P. Hobby and Robert E. Eberly. The Low Resolution Spectrograph 2 (LRS2) was developed and funded by the University of Texas at Austin McDonald Observatory and Department of Astronomy, and by Pennsylvania State University. We thank the Leibniz-Institut für Astrophysik Potsdam (AIP) and the Institut für Astrophysik Göttingen (IAG) for their contributions to the construction of the integral field units.

KAIT and its ongoing operation were made possible by donations from Sun Microsystems, Inc., the Hewlett-Packard Company, AutoScope Corporation, Lick Observatory, the US NSF, the University of California, the Sylvia & Jim Katzman Foundation, and the TABASGO Foundation. A major upgrade of the Kast spectrograph on the Shane 3 m telescope at Lick Observatory, led by Brad Holden, was made possible through generous gifts from the Heising-Simons Foundation, William and Marina Kast, and the University of California Observatories. Research at Lick Observatory is partially supported by a generous gift from Google. We would like to express our gratitude to the Lick Observatory staff for their support. Shane 3 m observations were conducted on the stolen land of the Ohlone (Costanoans), Tamyen, and Muwekma Ohlone tribes. We gratefully acknowledge the usage of native lands for our science. Observations from coauthor A.J.M. were made under the aegis of the ASTRAL (Astronomy/STEM Alliance with Lick Observatory) consortium, supported by a generous grant from the Gordon and Betty Moore Foundation (PI: B. Macintosh).

We thank the staff of IAO, Hanle, CREST, and Hosakote, who made these observations possible. The facilities at IAO and CREST are operated by the Indian Institute of Astrophysics, Bangalore. We thank the Subaru staff for the data taken by the Subaru Telescope (S23A-023). Based in part on observations made with the GTC, installed at the Spanish Observatorio del Roque de los Muchachos of the Instituto de Astrofísica de Canarias, on the island of La Palma, using OSIRIS and EMIR instruments.

Based (in part) on data acquired at the ANU 2.3 m telescope. The automation of the telescope was made possible through an initial grant provided by the Center of Gravitational Astrophysics and the Research School of Astronomy and Astrophysics at the Australian National University and through a grant provided by the Australian Research Council through LE230100063. We acknowledge the traditional custodians of the land on which the telescope stands, the Gamilaraay people, and pay our respects to elders past and present.

The HET is a joint project of the University of Texas at Austin, the Pennsylvania State University, Stanford University, Ludwig-Maximilians-Universität München, and Georg-August-Universität Göttingen. The HET is named in honor of its principal benefactors, William P. Hobby and

Robert E. Eberly. The Marcario Low-Resolution Spectrograph is named for Mike Marcario of High Lonesome Optics, who fabricated several optics for the instrument but died before its completion. The LRS is a joint project of the HET partnership and the Instituto de Astronomía de la Universidad Nacional Autónoma de México.

We acknowledge Weizmann Interactive Supernova data Repository (WISeREP) at https://www.wiserep.org (O. Yaron & A. Gal-Yam 2012). This research has made use of the CfA Supernova Archive, which is funded in part by the NSF through grant AST-0907903. This research has made use of the NASA/IPAC Extragalactic Database (NED), which is operated by the Jet Propulsion Laboratory, California Institute of Technology, under contract with NASA.

M.S. acknowledges financial support provided under the National Post Doctoral Fellowship (N-PDF; File No.: PDF/2023/002244) by the Science & Engineering Research Board (SERB), Anusandhan National Research Foundation (ANRF), Government of India. L.A.K. is supported by a CIERA Postdoctoral Fellowship.

Support for this research at Rutgers University (S.W.J., C.L., M.S.) was provided by NSF award AST-2407567.

A.A.M., C.L., and N.R. are supported by DoE award #DE-SC0025599. MMT and Keck Observatory access for N.R. and C.L. was supported by Northwestern University and the Center for Interdisciplinary Exploration and Research in Astrophysics (CIERA). A.C.G. and the Fong Group at Northwestern acknowledge support by the NSF under grants AST-1909358, AST-2206494, AST-2308182, and CAREER grant AST-2047919.

G.C.A. thanks the Indian National Science Academy for support under the INSA Senior Scientist Program. A.F. acknowledges support by the European Research Council (ERC) under the European Union's Horizon 2020 research and innovation program (ERC Advanced Grant KILONOVA #885281) and the State of Hesse within the Cluster Project ELEMENTS. C.L. acknowledges support from DOE award DE-SC0010008 to Rutgers University. M.R.S. is supported by the STScI Postdoctoral Fellowship.

Time-domain research by the University of Arizona team and D.J.S. is supported by NSF grants 2108032, 2308181, 2407566, and 2432036 and the Heising-Simons Foundation under grant #2020-1864. Time-domain research by the University of California, Davis team and S.V. is supported by NSF grant AST-2407565. K.A.B. is supported by an LSST-DA Catalyst Fellowship; this publication was thus made possible through the support of grant 62192 from the John Templeton Foundation to LSST-DA. N.F. acknowledges support from the NSF Graduate Research Fellowship Program under grant DGE-2137419.

J.E.A. is supported by the international Gemini Observatory, a program of NSF's NOIRLab, which is managed by the Association of Universities for Research in Astronomy (AURA) under a cooperative agreement with the NSF, on behalf of the Gemini partnership of Argentina, Brazil, Canada, Chile, the Republic of Korea, and the United States of America. J.A.V. acknowledges the Postgraduate School of the Universidad de Antofagasta for its support and allocated grants. R.D. acknowledges funds from ANID grant FONDECYT Postdoctorado #3220449.

A.V.F.'s group at UC Berkeley received financial assistance from the Christopher R. Redlich Fund, as well as donations from Gary and Cynthia Bengier, Clark and Sharon Winslow, Alan Eustace and Kathy Kwan, William Draper, Timothy and Melissa Draper, Briggs and Kathleen Wood, Sanford Robertson (W.Z. is a Bengier-Winslow-Eustace Specialist in Astronomy, T.G.B. is a Draper-Wood-Robertson Specialist in Astronomy, Y.Y. was a Bengier–Winslow–Robertson Fellow in Astronomy), and numerous other donors.

K. Maguire acknowledges funding from Horizon Europe ERC grant 101125877. J.H.T. acknowledges support from EU H2020 ERC grant 758638. T.T. acknowledges support from NSF grant AST-2205314 and the NASA ADAP award 80NSSC23K1130. K. Maede acknowledges support from JSPS KAKENHI grants JP24KK0070, JP24H01810, and JP20H00174, and from JSPS Bilateral Joint Research Project (JPJSBP120229923). K. Misra acknowledges support from the BRICS grant DST/ICD/BRICS/Call-5/CoNMuTraMO/2023 (G) funded by the DST, India. J.V. is supported by NKFIH-OTKA grant K142534. G.C.A. thanks the Indian National Science Academy for support under the INSA Senior Scientist Program. M.R.S. is supported by the STScI Postdoctoral Fellowship. B.B. received support from the Hungarian National Research, Development and Innovation Office grants OTKA PD-147091. L.G. acknowledges financial support from AGAUR, CSIC, MCIN, and AEI 10.13039/501100011033 under projects PID2023-151307NB-I00, PIE 20215AT016, CEX2020-001058-M, ILINK23001, COOPB2304, and 2021-SGR-01270. H.K. was funded by the Research Council of Finland projects 324504, 328898, and 353019. D.A.H., G.H., and C.M. were supported by NSF grants AST-1313484 and AST-1911225.

Appendix

Tables 3, 4, and 5 present the photometric observations from Swift, optical spectroscopic observations, and NIR observations of SN 2024pxl.

Table 3
UV and Optical Observations of SN 2024pxl

Date	JD[a]	Phase[b] (days)	*UVW*2 (mag)	*UVM*2 (mag)	*UVW*1 (mag)	Swift *U* (mag)	Swift *B* (mag)	Swift *V* (mag)
2024-07-26	518.17	−6.44	19.09 ± 0.20	19.88 ± 0.32	18.03 ± 0.14	16.50 ± 0.08	17.00 ± 0.07	16.71 ± 0.10
2024-07-28	519.90	−4.71	⋯	⋯	17.90 ± 0.14	16.18 ± 0.08	16.72 ± 0.07	⋯
2024-07-28	519.91	−4.70	19.34 ± 0.25	19.72 ± 0.32	⋯	⋯	⋯	16.28 ± 0.09
2024-07-31	523.09	−1.52	⋯	⋯	17.84 ± 0.13	16.31 ± 0.08	16.53 ± 0.06	⋯
2024-07-31	523.10	−1.51	19.05 ± 0.20	⋯	⋯	⋯	⋯	16.09 ± 0.08
2024-08-04	527.19	2.58	⋯	⋯	18.28 ± 0.16	16.57 ± 0.08	16.45 ± 0.06	⋯
2024-08-04	527.20	2.59	19.64 ± 0.28	⋯	⋯	⋯	⋯	15.99 ± 0.07
2024-08-07	530.09	5.48	⋯	20.01 ± 0.35	18.62 ± 0.20	17.05 ± 0.10	16.68 ± 0.07	15.87 ± 0.07
2024-08-10	533.17	8.56	⋯	⋯	19.03 ± 0.34	17.64 ± 0.17	17.06 ± 0.09	⋯
2024-08-10	533.18	8.57	⋯	⋯	⋯	⋯	⋯	16.00 ± 0.09
2024-08-13	536.39	11.78	⋯	⋯	⋯	⋯	17.51 ± 0.10	16.34 ± 0.09
2024-08-16	538.81	14.20	⋯	⋯	⋯	18.54 ± 0.27	⋯	⋯
2024-08-16	538.82	14.21	⋯	⋯	⋯	⋯	17.85 ± 0.12	⋯
2024-08-19	542.04	17.43	⋯	⋯	⋯	18.85 ± 0.26	18.67 ± 0.16	16.77 ± 0.09

Notes.
[a] JD 2,460,000+.
[b] Phase calculated with respect to $B_{max} = 2, 460, 524.61$.

Table 4
Log of Optical Spectroscopy of SN 2024pxl

Date	JD[a]	Phase[b] (days)	Telescope/Instrument
2024-07-24	515.84	−8.77	P200/DBSP
2024-07-26	517.95	−6.66	FTN/FLOYDS
2024-07-27	518.74	−5.87	HET/LRS
2024-07-27	518.83	−5.78	Gemini-N/GMOS-N
2024-07-27	518.9	−5.71	Lick/Kast
2024-07-28	519.76	−4.85	FTN/FLOYDS
2024-07-29	520.80	−3.81	FTN/FLOYDS
2024-07-29	520.90	−3.71	ANU/WiFeS
2024-07-30	521.87	−2.74	ANU/WiFeS
2024-07-30	522.29	−2.32	SALT/RSS
2024-07-31	522.75	−1.86	Lick/Kast
2024-07-31	523.29	−1.32	SALT/RSS
2024-08-01	523.73	−0.88	Lick/Kast
2024-08-01	523.78	−0.83	P200/DBSP
2024-08-01	523.79	−0.82	Keck/LRIS
2024-08-01	523.87	−0.74	ANU/WiFeS
2024-08-01	523.89	−0.72	FTN/FLOYDS
2024-08-01	524.30	−0.31	SALT/RSS
2024-08-02	524.92	0.31	ANU/WiFeS
2024-08-02	525.19	0.58	Lick/Kast
2024-08-03	525.83	1.22	FTN/FLOYDS
2024-08-05	527.79	3.18	FTN/FLOYDS
2024-08-05	527.79	3.18	HET/LRS
2024-08-05	528.29	3.68	SALT/RSS
2024-08-06	528.77	4.16	Lick/Kast
2024-08-06	528.88	4.27	FTN/FLOYDS
2024-08-06	528.92	4.31	LT/SPRAT
2024-08-06	528.93	4.32	ANU/WiFeS
2024-08-06	529.28	4.67	SALT/RSS
2024-08-07	530.20	5.59	Lick/Kast
2024-08-07	530.20	5.59	GTC/OSIRIS
2024-08-08	530.80	6.19	FTN/FLOYDS
2024-08-10	533.47	8.86	NOT/ALFOSC
2024-08-12	534.75	10.14	MMT/Binospec
2024-08-12	534.79	10.18	FTN/FLOYDS
2024-08-13	536.13	11.52	HCT/HFOSC
2024-08-14	536.81	12.20	FTN/FLOYDS
2024-08-14	537.27	12.66	SALT/RSS
2024-08-14	537.36	12.75	Lick/Kast

Table 4
(Continued)

Date	JD[a]	Phase[b] (days)	Telescope/Instrument
2024-08-14	537.41	12.80	NOT/ALFOSC
2024-08-15	537.79	13.18	HET/LRS
2024-08-15	537.90	13.29	LT/SPRAT
2024-08-15	538.36	13.75	SALT/RSS
2024-08-15	538.36	13.75	SALT/RSS
2024-08-16	538.74	14.13	P200/DBSP
2024-08-16	538.80	14.19	Lick/Kast
2024-08-18	540.82	16.21	FTN/FLOYDS
2024-08-19	541.88	17.27	ANU/WiFeS
2024-08-23	545.76	21.15	FTN/FLOYDS
2024-08-23	546.10	21.49	HCT/HFOSC
2024-08-23	546.43	21.82	NOT/ALFOSC
2024-08-23	546.43	21.82	SALT/RSS
2024-08-26	548.88	24.27	ANU/WiFeS
2024-08-27	549.75	25.14	Lick/Kast
2024-08-27	549.94	25.33	FTN/FLOYDS
2024-08-29	551.52	26.91	Lick/Kast
2024-08-31	553.66	29.05	MMT/Binospec
2024-08-31	553.73	29.12	Keck/LRIS
2024-08-31	553.93	29.32	FTN/FLOYDS
2024-09-02	555.83	31.22	Keck/LRIS
2024-09-04	557.88	33.27	FTN/FLOYDS
2024-09-05	558.52	33.91	GTC/OSIRIS
2024-09-05	558.92	34.31	ANU/WiFeS
2024-09-05	559.00	34.39	Lick/Kast
2024-09-05	559.49	34.88	VLT/XShooter
2024-09-06	559.92	35.31	NOT/ALFOSC
2024-09-06	560.35	35.74	NOT/ALFOSC
2024-09-08	561.65	37.04	MMT/Binospec
2024-09-08	561.71	37.10	Lick/Kast
2024-09-10	563.76	39.15	FTN/FLOYDS
2024-09-11	565.00	40.39	Lick/Kast
2024-09-13	566.67	42.06	Lick/Kast
2024-09-14	567.79	43.18	FTN/FLOYDS
2024-09-14	567.91	43.30	ANU/WiFeS
2024-09-18	571.72	47.11	FTN/FLOYDS
2024-09-21	575.36	50.75	NOT/ALFOSC
2024-09-23	576.87	52.26	FTN/FLOYDS
2024-09-28	581.79	57.18	Lick/Kast
2024-09-30	583.58	58.97	MMT/Binospec
2024-10-01	584.74	60.13	FTN/FLOYDS
2024-10-03	586.65	62.04	Lick/Kast
2024-10-04	587.92	63.31	Lick/Kast
2024-10-05	588.74	64.13	FTN/FLOYDS
2024-10-05	588.79	64.18	Keck/LRIS
2024-10-05	588.92	64.31	Lick/Kast
2024-10-05	589.00	64.39	NOT/ALFOSC
2024-10-05	589.37	64.76	NOT/ALFOSC
2024-10-08	591.79	67.18	Keck/LRIS
2024-10-10	593.91	69.31	Lick/Kast
2024-10-12	595.66	71.05	Lick/Kast
2024-10-19	602.72	78.11	FTN/FLOYDS
2024-10-24	607.63	83.02	Lick/Kast
2024-10-25	608.71	84.10	FTN/FLOYDS
2024-10-26	609.79	85.18	Lick/Kast
2024-10-30	613.70	89.09	Keck/LRIS

Notes.
[a] JD 2,460,000+.
[b] Phase calculated with respect to $B_{max} = 2, 460, 524.61$.

Table 5
Log of NIR Spectroscopy of SN 2024pxl

Date	JD[a]	Phase[b] (days)	Telescope/Instrument
2024-07-26	517.95	−6.66	Keck/NIRES
2024-07-28	520.63	−3.98	Magellan/FIRE
2024-08-10	532.95	8.34	Magellan/FIRE
2024-08-12	534.88	10.27	IRTF/SpeX
2024-08-19	542.43	17.82	GTC/EMIR
2024-08-26	548.02	23.41	Soar/TripleSpec
2024-09-05	559.49	34.88	VLT/XShooter[c]
2024-09-06	560.49	35.88	Soar/TripleSpec
2024-09-13	567.07	42.46	GTC/EMIR

Notes.
[a] JD 2,460,000+.
[b] Phase calculated with respect to B_{max} = 2, 460, 524.61.
[c] This is the same spectrum as referred to in Table 4.

Optical Photometry and Spectroscopy of SN 2017drh

We present the optical LCO photometry (Figure 21, Table 6) and FLOYDS spectroscopy (Figure 22, Table 7) for SN 2017drh, which exploded in the same host galaxy, NGC 6384, as SN 2024pxl. The spectra were reduced using the `FLOYDS` reduction pipeline (S. Valenti et al. 2014). The photometric observations were taken as part of the GSP collaboration. These data were reduced with `lcogtsnpipe` (S. Valenti et al. 2016), a PyRAF-based image-reduction pipeline (Table 6). In Figure 21, the LCO data are shown with the BayeSN light curve fits that also included data from B. E. Stahl et al. (2019).

Table 6
Photometric Observations of SN 2017drh

Date	JD[a]	Phase[b] (days)	U (mag)	B (mag)	g (mag)	V (mag)	r (mag)	i (mag)
2017-05-10	883.54	−7.66	18.51 ± 0.26	17.46 ± 0.03	⋯	⋯	⋯	⋯
2017-05-10	883.55	−7.65	⋯	17.52 ± 0.05	17.16 ± 0.02	16.35 ± 0.02	⋯	⋯
2017-05-10	883.56	−7.64	⋯	⋯	17.15 ± 0.02	⋯	15.74 ± 0.01	15.27 ± 0.02
2017-05-13	887.48	−3.72	18.37 ± 0.08	⋯	⋯	⋯	⋯	⋯
2017-05-13	887.49	−3.71	18.41 ± 0.08	17.09 ± 0.03	⋯	⋯	⋯	⋯
2017-05-14	887.50	−3.70	⋯	17.07 ± 0.04	16.73 ± 0.02	15.87 ± 0.02	⋯	⋯
2017-05-14	887.51	−3.69	⋯	⋯	⋯	⋯	15.35 ± 0.01	14.99 ± 0.01
2017-05-15	888.53	−2.67	18.01 ± 0.21	⋯	⋯	⋯	⋯	⋯
2017-05-15	888.54	−2.66	17.96 ± 0.19	16.99 ± 0.04	⋯	⋯	⋯	⋯
2017-05-15	888.55	−2.65	⋯	⋯	16.59 ± 0.04	15.98 ± 0.02	⋯	⋯
2017-05-15	888.56	−2.64	⋯	⋯	⋯	⋯	15.25 ± 0.02	14.97 ± 0.03
2017-05-16	889.56	−1.64	18.69 ± 0.09	⋯	⋯	⋯	⋯	⋯
2017-05-16	890.47	−0.73	18.32 ± 0.07	⋯	⋯	⋯	⋯	⋯
2017-05-16	890.48	−0.72	⋯	16.95 ± 0.03	⋯	15.75 ± 0.02	⋯	⋯
2017-05-18	891.50	0.30	18.41 ± 0.06	⋯	⋯	⋯	⋯	⋯
2017-05-18	891.51	0.31	18.40 ± 0.06	17.06 ± 0.02	⋯	15.86 ± 0.02	⋯	⋯
2017-05-18	891.52	0.32	⋯	⋯	16.63 ± 0.01	15.81 ± 0.01	15.28 ± 0.01	⋯
2017-05-18	891.53	0.33	⋯	⋯	⋯	⋯	15.28 ± 0.01	15.16 ± 0.01
2017-05-18	892.45	1.25	18.11 ± 0.19	⋯	⋯	⋯	⋯	⋯
2017-05-18	892.46	1.26	⋯	16.98 ± 0.02	⋯	15.76 ± 0.01	⋯	⋯
2017-05-18	892.47	1.27	⋯	⋯	16.61 ± 0.01	⋯	15.26 ± 0.01	⋯
2017-05-18	892.48	1.28	⋯	⋯	⋯	⋯	⋯	15.15 ± 0.01
2017-05-21	895.49	4.29	18.21 ± 0.18	⋯	⋯	⋯	⋯	⋯
2017-05-22	895.50	4.30	18.23 ± 0.18	17.21 ± 0.03	⋯	⋯	⋯	⋯
2017-05-22	895.51	4.31	⋯	⋯	16.69 ± 0.01	15.80 ± 0.02	⋯	⋯
2017-05-22	895.52	4.32	⋯	⋯	⋯	⋯	15.31 ± 0.01	15.24 ± 0.01
2017-05-22	896.19	4.99	18.76 ± 0.07	⋯	⋯	⋯	⋯	⋯
2017-05-22	896.20	5.00	18.70 ± 0.08	17.08 ± 0.02	⋯	⋯	⋯	⋯
2017-05-22	896.21	5.01	⋯	17.23 ± 0.02	16.63 ± 0.01	15.84 ± 0.02	⋯	⋯
2017-05-22	896.22	5.02	⋯	⋯	16.62 ± 0.01	⋯	15.27 ± 0.01	15.23 ± 0.01
2017-05-23	897.19	5.99	18.55 ± 0.21	⋯	⋯	⋯	⋯	⋯
2017-05-23	897.20	6.00	⋯	17.45 ± 0.03	⋯	16.02 ± 0.02	⋯	⋯
2017-05-23	897.21	6.01	⋯	⋯	16.71 ± 0.01	15.86 ± 0.01	15.32 ± 0.05	⋯

Table 6
(Continued)

Date	JD[a]	Phase[b] (days)	U (mag)	B (mag)	g (mag)	V (mag)	r (mag)	i (mag)
2017-05-23	897.22	6.02	⋯	⋯	⋯	⋯	15.33 ± 0.01	⋯
2017-05-26	900.20	9.00	19.21 ± 0.08	⋯	⋯	⋯	⋯	⋯
2017-05-26	900.21	9.01	18.98 ± 0.32	17.45 ± 0.03	⋯	⋯	⋯	⋯
2017-05-26	900.22	9.02	⋯	⋯	16.82 ± 0.01	16.07 ± 0.02	⋯	⋯
2017-05-26	900.23	9.03	⋯	⋯	⋯	⋯	15.55 ± 0.01	15.53 ± 0.01
2017-05-31	905.18	13.98	19.08 ± 0.34	⋯	⋯	⋯	⋯	⋯
2017-05-31	905.19	13.99	⋯	18.38 ± 0.04	⋯	⋯	⋯	⋯
2017-05-31	905.20	14.00	⋯	⋯	17.33 ± 0.02	16.42 ± 0.02	⋯	⋯
2017-05-31	905.21	14.01	⋯	⋯	⋯	⋯	15.81 ± 0.01	15.54 ± 0.01
2017-06-05	910.37	19.17	20.21 ± 0.35	⋯	⋯	⋯	⋯	⋯
2017-06-05	910.38	19.18	20.37 ± 0.30	18.64 ± 0.12	⋯	⋯	⋯	⋯
2017-06-05	910.39	19.19	⋯	⋯	18.00 ± 0.04	16.61 ± 0.03	⋯	⋯
2017-06-05	910.40	19.20	⋯	⋯	⋯	⋯	15.96 ± 0.02	15.51 ± 0.02
2017-06-09	913.73	22.53	⋯	⋯	⋯	⋯	16.04 ± 0.03	⋯
2017-06-09	913.74	22.54	⋯	⋯	⋯	16.91 ± 0.04	⋯	⋯
2017-06-09	913.75	22.55	⋯	18.97 ± 0.22	⋯	16.80 ± 0.04	⋯	⋯
2017-06-09	913.76	22.56	⋯	19.21 ± 0.25	⋯	⋯	⋯	⋯
2017-06-15	919.88	28.68	⋯	⋯	18.72 ± 0.07	⋯	16.53 ± 0.03	⋯
2017-06-15	919.89	28.69	⋯	18.76 ± 0.23	18.96 ± 0.15	⋯	⋯	⋯
2017-06-15	920.06	28.86	⋯	⋯	18.83 ± 0.06	17.49 ± 0.04	⋯	⋯
2017-06-15	920.07	28.87	⋯	⋯	⋯	⋯	16.43 ± 0.04	⋯
2017-06-15	920.08	28.88	⋯	⋯	18.75 ± 0.09	⋯	⋯	⋯
2017-06-15	920.09	28.89	⋯	19.56 ± 0.18	⋯	17.51 ± 0.04	⋯	⋯
2017-06-15	920.10	28.90	20.63 ± 0.35	⋯	⋯	⋯	⋯	⋯
2017-06-15	920.11	28.91	⋯	⋯	⋯	⋯	16.55 ± 0.02	15.87 ± 0.02
2017-06-22	927.07	35.87	⋯	19.71 ± 0.07	⋯	⋯	⋯	⋯
2017-06-22	927.08	35.88	⋯	19.82 ± 0.07	⋯	17.91 ± 0.05	⋯	16.31 ± 0.03
2017-06-22	927.09	35.89	⋯	⋯	19.04 ± 0.06	⋯	16.94 ± 0.06	⋯
2017-06-26	931.11	39.91	20.98 ± 0.48	⋯	⋯	⋯	⋯	⋯
2017-06-26	931.12	39.92	20.25 ± 0.43	⋯	⋯	⋯	⋯	⋯
2017-06-26	931.13	39.93	⋯	19.64 ± 0.23	19.07 ± 0.11	17.83 ± 0.09	⋯	⋯
2017-06-26	931.14	39.94	⋯	⋯	18.98 ± 0.07	⋯	17.05 ± 0.03	16.48 ± 0.06
2017-06-26	931.15	39.95	⋯	⋯	⋯	⋯	⋯	16.61 ± 0.12
2017-06-28	932.83	41.63	19.72 ± 0.43	⋯	⋯	⋯	⋯	⋯
2017-06-28	932.84	41.64	19.93 ± 0.54	19.69 ± 0.18	⋯	⋯	⋯	⋯
2017-06-28	932.85	41.65	⋯	19.80 ± 0.17	⋯	17.84 ± 0.05	⋯	16.62 ± 0.03
2017-06-28	932.86	41.66	⋯	⋯	⋯	⋯	⋯	16.63 ± 0.02
2017-06-30	934.85	43.65	⋯	⋯	⋯	18.00 ± 0.03	⋯	⋯
2017-07-01	935.61	44.41	21.06 ± 0.26	⋯	⋯	⋯	⋯	⋯
2017-07-01	935.62	44.42	21.01 ± 0.21	19.94 ± 0.13	⋯	⋯	⋯	⋯
2017-07-01	935.63	44.43	⋯	19.86 ± 0.16	19.38 ± 0.07	18.00 ± 0.05	⋯	⋯
2017-07-01	935.64	44.44	⋯	⋯	19.41 ± 0.07	⋯	17.40 ± 0.03	16.85 ± 0.03
2017-07-01	935.65	44.45	⋯	⋯	⋯	⋯	⋯	16.85 ± 0.03
2017-07-03	938.43	47.23	⋯	19.85 ± 0.19	⋯	⋯	⋯	⋯
2017-07-03	938.44	47.24	⋯	20.25 ± 0.17	⋯	17.98 ± 0.05	⋯	⋯
2017-07-03	938.45	47.25	⋯	⋯	19.50 ± 0.10	⋯	17.49 ± 0.03	⋯
2017-07-03	938.46	47.26	⋯	⋯	⋯	⋯	17.47 ± 0.03	16.90 ± 0.03
2017-07-09	943.67	52.47	⋯	20.39 ± 0.35	⋯	⋯	⋯	⋯
2017-07-09	943.68	52.48	⋯	⋯	19.12 ± 0.26	18.23 ± 0.08	⋯	⋯
2017-07-09	943.69	52.49	⋯	⋯	18.65 ± 0.22	⋯	17.42 ± 0.14	⋯
2017-07-09	943.70	52.50	⋯	⋯	⋯	⋯	⋯	16.93 ± 0.12
2017-07-15	950.05	58.85	⋯	19.80 ± 0.19	⋯	⋯	⋯	⋯
2017-07-15	950.06	58.86	⋯	⋯	19.59 ± 0.12	18.24 ± 0.06	⋯	⋯
2017-07-15	950.07	58.87	⋯	⋯	19.51 ± 0.11	⋯	17.78 ± 0.03	⋯
2017-07-15	950.08	58.88	⋯	⋯	⋯	⋯	⋯	17.32 ± 0.04
2017-07-21	956.29	65.09	⋯	20.26 ± 0.08	⋯	⋯	⋯	⋯
2017-07-21	956.30	65.10	⋯	20.29 ± 0.08	⋯	18.50 ± 0.03	⋯	⋯
2017-07-21	956.31	65.11	⋯	⋯	19.78 ± 0.11	⋯	18.12 ± 0.05	⋯
2017-07-21	956.32	65.12	⋯	⋯	⋯	⋯	18.14 ± 0.05	17.59 ± 0.05
2017-07-27	962.34	71.14	⋯	20.39 ± 0.10	⋯	⋯	⋯	⋯
2017-07-27	962.35	71.15	⋯	⋯	19.74 ± 0.09	18.65 ± 0.04	⋯	⋯
2017-07-27	962.36	71.16	⋯	⋯	19.70 ± 0.10	⋯	18.31 ± 0.05	⋯
2017-07-27	962.37	71.17	⋯	⋯	⋯	⋯	⋯	17.82 ± 0.06

Table 6
(Continued)

Date	JD[a]	Phase[b] (days)	U (mag)	B (mag)	g (mag)	V (mag)	r (mag)	i (mag)
2017-08-02	968.32	77.12	⋯	20.65 ± 0.38	⋯	⋯	⋯	⋯
2017-08-02	968.33	77.13	⋯	20.88 ± 0.48	⋯	18.65 ± 0.11	⋯	⋯
2017-08-02	968.34	77.14	⋯	⋯	20.09 ± 0.18	⋯	18.47 ± 0.09	⋯
2017-08-02	968.35	77.15	⋯	⋯	⋯	⋯	18.59 ± 0.10	⋯
2017-08-08	973.98	82.78	⋯	19.86 ± 0.21	⋯	⋯	⋯	⋯
2017-08-08	973.99	82.79	⋯	⋯	19.53 ± 0.13	19.36 ± 0.18	⋯	⋯
2017-08-08	974.00	82.80	⋯	⋯	20.04 ± 0.14	⋯	18.50 ± 0.11	⋯
2017-08-08	974.01	82.81	⋯	⋯	⋯	⋯	⋯	18.16 ± 0.11
2017-08-14	979.98	88.78	⋯	20.15 ± 0.21	⋯	⋯	⋯	⋯
2017-08-14	979.99	88.79	⋯	20.58 ± 0.14	⋯	18.96 ± 0.10	⋯	⋯
2017-08-14	980.00	88.80	⋯	⋯	19.18 ± 0.26	⋯	⋯	⋯
2017-08-19	984.55	93.35	⋯	20.03 ± 0.14	⋯	⋯	⋯	⋯
2017-08-19	984.56	93.36	⋯	20.66 ± 0.18	⋯	19.27 ± 0.10	⋯	⋯
2017-08-19	984.57	93.37	⋯	⋯	19.98 ± 0.09	⋯	19.24 ± 0.10	⋯
2017-08-19	984.58	93.38	⋯	⋯	⋯	⋯	19.31 ± 0.11	18.60 ± 0.10
2017-08-25	990.56	99.36	⋯	20.26 ± 0.18	⋯	19.38 ± 0.08	⋯	⋯
2017-08-25	990.57	99.37	⋯	⋯	20.02 ± 0.11	19.52 ± 0.07	⋯	⋯
2017-08-25	990.58	99.38	⋯	⋯	⋯	⋯	19.26 ± 0.10	18.79 ± 0.10
2017-08-25	990.59	99.39	⋯	⋯	⋯	⋯	⋯	18.88 ± 0.09
2017-08-31	996.94	105.74	⋯	19.53 ± 0.09	⋯	19.32 ± 0.09	⋯	⋯
2017-08-31	996.95	105.75	⋯	⋯	19.86 ± 0.10	20.44 ± 0.50	⋯	⋯
2017-08-31	996.96	105.76	⋯	⋯	⋯	⋯	19.35 ± 0.09	19.09 ± 0.11
2017-08-31	996.97	105.77	⋯	⋯	⋯	⋯	⋯	19.93 ± 0.22
2017-09-06	1002.92	111.72	⋯	21.22 ± 0.32	⋯	⋯	⋯	⋯
2017-09-06	1002.93	111.73	⋯	⋯	20.37 ± 0.13	19.72 ± 0.25	⋯	⋯
2017-09-06	1002.94	111.74	⋯	⋯	20.61 ± 0.19	⋯	20.00 ± 0.16	⋯
2017-09-06	1002.95	111.75	⋯	⋯	⋯	⋯	⋯	19.10 ± 0.16
2017-09-12	1008.63	117.43	⋯	20.83 ± 0.15	⋯	⋯	⋯	⋯
2017-09-12	1008.64	117.44	⋯	⋯	20.07 ± 0.13	19.87 ± 0.18	⋯	⋯
2017-09-12	1008.65	117.45	⋯	⋯	20.50 ± 0.17	⋯	19.87 ± 0.13	⋯
2017-09-12	1008.66	117.46	⋯	⋯	⋯	⋯	⋯	19.24 ± 0.13
2017-09-16	1012.88	121.68	⋯	20.35 ± 0.21	⋯	⋯	⋯	⋯
2017-09-16	1012.89	121.69	⋯	⋯	21.08 ± 0.14	19.82 ± 0.14	⋯	⋯
2017-09-16	1012.90	121.70	⋯	⋯	20.07 ± 0.11	⋯	⋯	⋯
2017-09-16	1012.91	121.71	⋯	⋯	⋯	⋯	20.18 ± 0.20	19.53 ± 0.17
2017-09-16	1012.92	121.72	⋯	⋯	⋯	⋯	⋯	19.46 ± 0.17
2017-10-09	1035.59	144.39	⋯	21.34 ± 0.17	⋯	⋯	⋯	⋯
2017-10-09	1035.60	144.40	⋯	⋯	⋯	20.29 ± 0.10	⋯	⋯
2017-10-09	1035.61	144.41	⋯	⋯	20.78 ± 0.12	⋯	⋯	⋯
2017-10-09	1035.62	144.42	⋯	⋯	⋯	⋯	20.55 ± 0.19	20.10 ± 0.25
2017-10-09	1035.63	144.43	⋯	⋯	⋯	⋯	⋯	21.80 ± 0.48
2017-10-17	1043.56	152.36	⋯	21.72 ± 0.40	⋯	⋯	⋯	⋯
2017-10-17	1043.57	152.37	⋯	21.47 ± 0.25	⋯	20.61 ± 0.15	⋯	⋯
2017-10-17	1043.58	152.38	⋯	⋯	⋯	20.19 ± 0.12	⋯	⋯
2017-10-17	1043.59	152.39	⋯	⋯	21.67 ± 0.14	⋯	20.37 ± 0.21	⋯
2017-10-17	1043.60	152.40	⋯	⋯	⋯	⋯	20.61 ± 0.19	19.87 ± 0.22
2018-03-07	1184.92	293.72	⋯	21.15 ± 0.44	⋯	⋯	⋯	⋯
2018-03-07	1184.93	293.73	⋯	20.96 ± 0.42	⋯	⋯	⋯	⋯
2018-03-07	1184.94	293.74	⋯	⋯	⋯	21.46 ± 0.45	⋯	⋯
2018-03-07	1184.95	293.75	⋯	⋯	22.27 ± 0.30	21.19 ± 0.41	⋯	⋯
2018-03-07	1184.96	293.76	⋯	⋯	23.12 ± 0.31	⋯	⋯	⋯
2018-03-07	1184.97	293.77	⋯	⋯	⋯	⋯	22.14 ± 0.16	⋯
2018-03-07	1184.98	293.78	⋯	⋯	⋯	⋯	⋯	21.41 ± 0.23
2018-03-07	1184.99	293.79	⋯	⋯	⋯	⋯	⋯	21.70 ± 0.24

Notes.
[a] JD 2,457,000+.
[b] Phase calculated with respect to $B_{max} = 2, 457, 891.2$.

Table 7
Log of Spectroscopy of SN 2017drh

Date	JD[a]	Phase[b] (days)	Telescope/Instrument
2017-05-03	877.07	−14.12	FTN/FLOYDS
2017-05-09	883.19	−8.00	FTN/FLOYDS
2017-05-15	889.21	−1.98	FTN/FLOYDS
2017-05-19	893.05	1.86	FTN/FLOYDS
2017-05-25	899.06	7.86	FTN/FLOYDS
2017-05-31	905.04	13.85	FTN/FLOYDS
2017-06-06	911.06	19.86	FTN/FLOYDS
2017-06-27	932.01	40.81	FTN/FLOYDS

Notes.
[a] JD 2,457,000+.
[b] Phase calculated with respect to $B_{\max} = 2, 457, 891.20$.

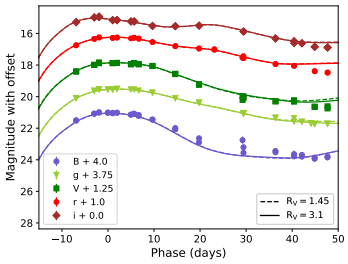

Figure 21. LCO light curves of 2017drh with offsets. The overplotted solid curve corresponds to the BayeSN model where $R_V = 3.1$, while the dashed curve represents the BayeSN model with $R_V = 1.45$. Unfortunately, without NIR data, we cannot distinguish well between the two models. The phases are given in the rest frame of SN 2017drh.

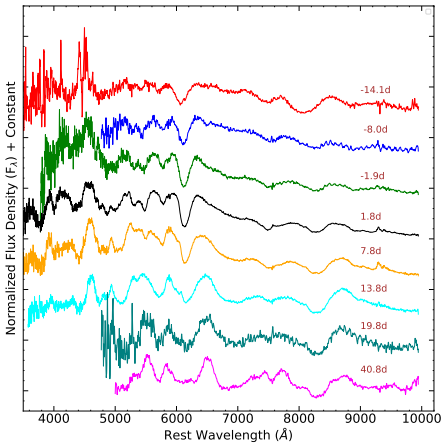

Figure 22. FTN/FLOYDS spectra of 2017drh from a phase of −14.1 to 40.8 days. A full list of spectroscopic observations is presented in Table 7. The nine optical spectra shown in this Figure are available in machine-readable format in a .tar.gz package.
(The data used to create this figure are available in the online article.)

ORCID iDs

Mridweeka Singh https://orcid.org/0000-0001-6706-2749
Lindsey A. Kwok https://orcid.org/0000-0003-3108-1328
Saurabh W. Jha https://orcid.org/0000-0001-8738-6011
R. Dastidar https://orcid.org/0000-0001-6191-7160
Conor Larison https://orcid.org/0000-0003-2037-4619
Alexei V. Filippenko https://orcid.org/0000-0003-3460-0103
Jennifer E. Andrews https://orcid.org/0000-0003-0123-0062
Moira Andrews https://orcid.org/0000-0002-1895-6639
G. C. Anupama https://orcid.org/0000-0003-3533-7183
Prasiddha Arunachalam https://orcid.org/0000-0002-6688-3307
Katie Auchettl https://orcid.org/0000-0002-4449-9152
Barnabas Barna https://orcid.org/0000-0003-4769-4794
K. Azalee Bostroem https://orcid.org/0000-0002-4924-444X
Thomas G. Brink https://orcid.org/0000-0001-5955-2502
Régis Cartier https://orcid.org/0000-0003-4553-4033
Ping Chen https://orcid.org/0000-0003-0853-6427
Collin T. Christy https://orcid.org/0000-0003-0528-202X
David A. Coulter https://orcid.org/0000-0003-4263-2228
Sofia Covarrubias https://orcid.org/0000-0003-1858-561X
Kyle W. Davis https://orcid.org/0000-0002-5680-4660
Connor B. Dickinson https://orcid.org/0000-0001-9749-4200
Yize Dong https://orcid.org/0000-0002-7937-6371
Joseph Farah https://orcid.org/0000-0003-4914-5625
Andreas Flörs https://orcid.org/0000-0003-2024-2819
Ryan J. Foley https://orcid.org/0000-0002-2445-5275
Noah Franz https://orcid.org/0000-0003-4537-3575
Christoffer Fremling https://orcid.org/0000-0002-4223-103X
Lluís Galbany https://orcid.org/0000-0002-1296-6887
Anjasha Gangopadhyay https://orcid.org/0000-0002-3884-5637
Aarna Garg https://orcid.org/0009-0002-4441-3192
Elinor L. Gates https://orcid.org/0000-0002-3739-0423
Or Graur https://orcid.org/0000-0002-4391-6137
Alexa C. Gordon https://orcid.org/0000-0002-5025-4645
Daichi Hiramatsu https://orcid.org/0000-0002-1125-9187
Emily Hoang https://orcid.org/0000-0003-2744-4755
D. Andrew Howell https://orcid.org/0000-0003-4253-656X
Brian Hsu https://orcid.org/0000-0002-9454-1742
Joel Johansson https://orcid.org/0000-0001-5975-290X
Arti Joshi https://orcid.org/0000-0001-9275-0287
Lordrick A. Kahinga https://orcid.org/0009-0007-5296-4046
Ravjit Kaur https://orcid.org/0009-0005-1871-7856
Sahana Kumar https://orcid.org/0000-0001-8367-7591
Piramon Kumnurdmanee https://orcid.org/0009-0004-7572-5679
Hanindyo Kuncarayakti https://orcid.org/0000-0002-1132-1366
Natalie LeBaron https://orcid.org/0000-0002-2249-0595
C. Lidman https://orcid.org/0000-0003-1731-0497
Chang Liu https://orcid.org/0000-0002-7866-4531
Keiichi Maeda https://orcid.org/0000-0003-2611-7269
Kate Maguire https://orcid.org/0000-0002-9770-3508
Bailey Martin https://orcid.org/0009-0006-4963-3206
Curtis McCully https://orcid.org/0000-0001-5807-7893
Darshana Mehta https://orcid.org/0009-0008-9693-4348
Luca M. Menotti https://orcid.org/0000-0001-7771-4624
Anne J. Metevier https://orcid.org/0009-0007-8154-6863
A. A. Miller https://orcid.org/0000-0001-9515-478X
Kuntal Misra https://orcid.org/0000-0003-1637-267X
C. Tanner Murphey https://orcid.org/0009-0006-5214-0736
Megan Newsome https://orcid.org/0000-0001-9570-0584
Estefania Padilla Gonzalez https://orcid.org/0000-0003-0209-9246

Kishore C. Patra https://orcid.org/0000-0002-1092-6806
Jeniveve Pearson https://orcid.org/0000-0002-0744-0047
Anthony L. Piro https://orcid.org/0000-0001-6806-0673
Abigail Polin https://orcid.org/0000-0002-1633-6495
Aravind P. Ravi https://orcid.org/0000-0002-7352-7845
Armin Rest https://orcid.org/0000-0002-4410-5387
Nabeel Rehemtulla https://orcid.org/0000-0002-5683-2389
Nicolas Meza Retamal https://orcid.org/0000-0002-7015-3446
O. M. Robinson https://orcid.org/0009-0006-3342-6181
César Rojas-Bravo https://orcid.org/0000-0002-7559-315X
Devendra K. Sahu https://orcid.org/0000-0002-6688-0800
David J. Sand https://orcid.org/0000-0003-4102-380X
Brian P. Schmidt https://orcid.org/0000-0002-8538-9195
Steve Schulze https://orcid.org/0000-0001-6797-1889
Michaela Schwab https://orcid.org/0009-0002-5096-1689
Manisha Shrestha https://orcid.org/0000-0002-4022-1874
Matthew R. Siebert https://orcid.org/0000-0003-2445-3891
Sunil Simha https://orcid.org/0000-0003-3801-1496
Nathan Smith https://orcid.org/0000-0001-5510-2424
Jesper Sollerman https://orcid.org/0000-0003-1546-6615
Shubham Srivastav https://orcid.org/0000-0003-4524-6883
Bhagya M. Subrayan https://orcid.org/0000-0001-8073-8731
Tamás Szalai https://orcid.org/0000-0003-4610-1117
Kirsty Taggart https://orcid.org/0000-0002-5748-4558
Rishabh Singh Teja https://orcid.org/0000-0002-0525-0872
Jacco H. Terwel https://orcid.org/0000-0001-9834-3439
Samaporn Tinyanont https://orcid.org/0000-0002-1481-4676
Stefano Valenti https://orcid.org/0000-0001-8818-0795
József Vinkó https://orcid.org/0000-0001-8764-7832
Aya L. Westerling https://orcid.org/0009-0003-8229-0127
J. Craig Wheeler https://orcid.org/0000-0003-1349-6538
Yi Yang https://orcid.org/0000-0002-6535-8500
WeiKang Zheng https://orcid.org/0000-0002-2636-6508

References

Amanullah, R., Johansson, J., Goobar, A., et al. 2015, MNRAS, 453, 3300
Arnett, W. D. 1982, ApJ, 253, 785
Bánhidi, D., Barna, B., Szalai, T., et al. 2025, A&A, 703, A64
Barna, B., Szalai, T., Jha, S. W., et al. 2021, MNRAS, 501, 1078
Bellm, E. C., Kulkarni, S. R., Barlow, T., et al. 2019b, PASP, 131, 068003
Bellm, E. C., Kulkarni, S. R., Graham, M. J., et al. 2019a, PASP, 131, 018002
Blagorodnova, N., Neill, J. D., Walters, R., et al. 2018, PASP, 130, 035003
Branch, D., Baron, E., Thomas, R. C., et al. 2004, PASP, 116, 903
Breeveld, A. A., Curran, P. A., Hoversten, E. A., et al. 2010, MNRAS, 406, 1687
Brown, T. M., Baliber, N., Bianco, F. B., et al. 2013, PASP, 125, 1031
Bulla, M., Goobar, A., & Dhawan, S. 2018, MNRAS, 479, 3663
Burns, C. R., Stritzinger, M., Phillips, M. M., et al. 2011, AJ, 141, 19
Camacho-Neves, Y., Jha, S. W., Barna, B., et al. 2023, ApJ, 951, 67
Cardiel, N., Pascual, S., Gallego, J., et al. 2019, ASPC, 523, 317
Carr, A., Davis, T. M., Camilleri, R., et al. 2024, PASA, 41, e068
Childress, M. J., Vogt, F. P. A., Nielsen, J., & Sharp, R. G. 2014, Ap&SS, 349, 617
Chonis, T. S., Hill, G. J., Lee, H., Tuttle, S. E., & Vattiat, B. L. 2014, SPIE, 9147, 91470A
Crawford, S. M., Still, M., Schellart, P., et al. 2010, SPIE, 7737, 773725
Cushing, M. C., Vacca, W. D., & Rayner, J. T. 2004, PASP, 116, 362
Das, H., Sahu, D., Dutta, A., et al. 2025, submitted
Dekany, R., Smith, R. M., Riddle, R., et al. 2020, PASP, 132, 038001
Dopita, M., Hart, J., McGregor, P., et al. 2007, Ap&SS, 310, 255
Dopita, M., Rhee, J., Farage, C., et al. 2010, Ap&SS, 327, 245
Drlica-Wagner, A., Carlin, J. L., Nidever, D. L., et al. 2021, ApJS, 256, 2
Dutta, A., Sahu, D. K., Anupama, G. C., et al. 2022, ApJ, 925, 217
Elias-Rosa, N., Benetti, S., Cappellaro, E., et al. 2006, MNRAS, 369, 1880
Elias-Rosa, N., Benetti, S., Turatto, M., et al. 2008, MNRAS, 384, 107
Fabricant, D., Fata, R., Epps, H., et al. 2019, PASP, 131, 075004
Filippenko, A. V. 1982, PASP, 94, 715
Filippenko, A. V. 2003, in From Twilight to Highlight: The Physics of Supernovae, ed. W. Hillebrandt & B. Leibundgut (Springer-Verlag), 171
Filippenko, A. V., Li, W. D., Treffers, R. R., & Modjaz, M. 2001, ASPC, 246, 121
Fink, M., Kromer, M., Seitenzahl, I. R., et al. 2014, MNRAS, 438, 1762
Flewelling, H. A., Magnier, E. A., Chambers, K. C., et al. 2020, ApJS, 251, 7
Foley, R. J., Challis, P. J., Chornock, R., et al. 2013, ApJ, 767, 57
Foley, R. J., Chornock, R., Filippenko, A. V., et al. 2009, AJ, 138, 376
Foley, R. J., Jha, S. W., Pan, Y.-C., et al. 2016, MNRAS, 461, 433
Foley, R. J., McCully, C., Jha, S. W., et al. 2014, ApJ, 792, 29
Foley, R. J., Rest, A., Stritzinger, M., et al. 2010, AJ, 140, 1321
Foley, R. J., Van Dyk, S. D., Jha, S. W., et al. 2015, ApJL, 798, L37
Freudling, W., Romaniello, M., Bramich, D. M., et al. 2013, A&A, 559, A96
Galbany, L., Gutiérrez, C. P., Piscarreta, L., et al. 2025, JCAP, 2025, 053
Ganeshalingam, M., Li, W., Filippenko, A. V., et al. 2010, ApJS, 190, 418
Gao, J., Jiang, B. W., Li, A., Li, J., & Wang, X. 2015, ApJL, 807, L26
Garzón, F., Balcells, M., Gallego, J., et al. 2022, A&A, 667, A107
Gehrels, N., Chincarini, G., Giommi, P., et al. 2004, ApJ, 611, 1005
Goobar, A. 2008, ApJL, 686, L103
Graham, M. J., Kulkarni, S. R., Bellm, E. C., et al. 2019, PASP, 131, 078001
Grayling, M., Thorp, S., Mandel, K. S., et al. 2024, MNRAS, 531, 953
Guevel, D., & Hosseinzadeh, G. 2017, Dguevel/Pyzogy: Initial Release, v0.0.1,, Zenodo, doi:10.5281/zenodo.1043973
Guy, J., Astier, P., Baumont, S., et al. 2007, A&A, 466, 11
Hoogendam, W. B., Ashall, C., Jones, D. O., et al. 2025, ApJ, 988, 209
Hook, I. M., Jørgensen, I., Allington-Smith, J. R., et al. 2004, PASP, 116, 425
Jha, S. W. 2017, in Handbook of Supernovae, ed. A. W. Alsabti & P. Murdin (Springer), 375
Jordan, G. C., IV, Perets, H. B., Fisher, R. T., & van Rossum, D. R. 2012, ApJL, 761, L23
Kamennoff, N., Foucaud, S., Reybier, S., Tsai, M.-F., & Tang, C.-H. 2012, ASPC, 461, 541
Kansky, J., Chilingarian, I., Fabricant, D., et al. 2019, PASP, 131, 075005
Karambelkar, V. R., Kasliwal, M. M., Maguire, K., et al. 2021, ApJL, 921, L6
Kawabata, K. S., Akitaya, H., Yamanaka, M., et al. 2014, ApJL, 795, L4
Kilpatrick, C. D., Foley, R. J., Drout, M. R., et al. 2018, MNRAS, 473, 4805
Kim, Y. L., Rigault, M., Neill, J. D., et al. 2022, PASP, 134, 024505
Krisciunas, K., Prieto, J. L., Garnavich, P. M., et al. 2006, AJ, 131, 1639
Kromer, M., Fink, M., Stanishev, V., et al. 2013, MNRAS, 429, 2287
Kromer, M., Ohlmann, S. T., Pakmor, R., et al. 2015, MNRAS, 450, 3045
Kwok, L. A., Singh, M., Jha, S. W., et al. 2025, ApJL, 989, L33
Lach, F., Callan, F. P., Bubeck, D., et al. 2022, A&A, 658, A179
Lagattuta, D. J., Mould, J. R., Staveley-Smith, L., et al. 2013, ApJ, 771, 88
Landolt, A. U. 1992, AJ, 104, 340
Li, L., Wang, X., Zhang, J., et al. 2018, MNRAS, 478, 4575
Li, W., Filippenko, A. V., Chornock, R., et al. 2003, PASP, 115, 453
Maeda, K., & Kawabata, M. 2022, ApJ, 941, 15
Magee, M. R., Killestein, T. L., Pursiainen, M., et al. 2025, MNRAS, 543, 3731
Magee, M. R., Kotak, R., Sim, S. A., et al. 2016, A&A, 589, A89
Magee, M. R., Kotak, R., Sim, S. A., et al. 2017, A&A, 601, A62
Maguire, K., Magee, M. R., Leloudas, G., et al. 2023, MNRAS, 525, 1210
Mandel, K. S., Thorp, S., Narayan, G., Friedman, A. S., & Avelino, A. 2022, MNRAS, 510, 3939
Mandigo-Stoba, M. S., Fremling, C., & Kasliwal, M. M. 2022a, JOSS, 7, 3612
Mandigo-Stoba, M. S., Fremling, C., & Kasliwal, M. M. 2022b, DBSP_DRP: A Python package for automated spectroscopic data reduction of DBSP data, Zenodo, doi:10.5281/zenodo.6241526
Masci, F. J., Laher, R. R., Rusholme, B., et al. 2019, PASP, 131, 018003
McClelland, C. M., Garnavich, P. M., Galbany, L., et al. 2010, ApJ, 720, 704
McCully, C., Jha, S. W., Foley, R. J., et al. 2014a, ApJ, 786, 134
McCully, C., Jha, S. W., Foley, R. J., et al. 2014b, Natur, 512, 54
McCully, C., Jha, S. W., Scalzo, R. A., et al. 2022, ApJ, 925, 138
McCully, C., Volgenau, N. H., Harbeck, D.-R., et al. 2018, SPIE, 10707, 107070K
Meng, X., & Podsiadlowski, P. 2014, ApJL, 789, L45
Miller, J. S., & Stone, R. P. S. 1994, The Kast Double Spectrograph: Lick Observatory Technical Reports No. 66, Univ. California
Milne, P. A., Brown, P. J., Roming, P. W. A., et al. 2010, ApJ, 721, 1627
Misra, K., Sahu, D. K., Anupama, G. C., & Pandey, K. 2008, MNRAS, 389, 706
Narayan, G., Foley, R. J., Berger, E., et al. 2011, ApJL, 731, L11

Nicholl, M. 2018, RNAAS, 2, 230
Nugent, P. E., Sullivan, M., Cenko, S. B., et al. 2011, Natur, 480, 344
Oke, J. B., & Gunn, J. E. 1982, PASP, 94, 586
Oke, J. B., & Gunn, J. E. 1983, ApJ, 266, 713
Oke, J. B., Cohen, J. G., Carr, M., et al. 1995, PASP, 107, 375
Pascual, S., Gallego, J., Cardiel, N., & Eliche-Moral, M. C. 2010, ASPC, 434, 353
Perley, D. A. 2019, PASP, 131, 084503
Phillips, M. M. 1993, ApJL, 413, L105
Phillips, M. M., Lira, P., Suntzeff, N. B., et al. 1999, AJ, 118, 1766
Phillips, M. M., Li, W., Frieman, J. A., et al. 2007, PASP, 119, 360
Piascik, A. S., Steele, I. A., Bates, S. D., et al. 2014, SPIE, 9147, 91478H
Prabhu, T. P., & Anupama, G. C. 2010, in Interstellar Matter and Star Formation: A Multi-wavelength Perspective, ASI Conf. Series, Vol. 1, ed. D. K. Ojha (Astronomical Society of India), 193
Prochaska, J. X., Hennawi, J. F., Westfall, K. B., et al. 2020, JOSS, 5, 2308
Prochaska, J. X., Hennawi, J., Cooke, R., et al. 2020, pypeit/PypeIt: Release 1.0.0, v1.0.0, Zenodo, doi:10.5281/zenodo.3743493
Prochaska, J. X., Hennawi, J. F., Cooke, R. J., et al. 2021, PypeIt: The Python Spectroscopic Data Reduction Pipeline (v1.6.0), 1.6.0,, Zenodo, doi:10.5281/zenodo.5548381
Ramsey, L. W., Adams, M. T., Barnes, T. G., et al. 1998, SPIE, 3352, 34
Rayner, J. T., Toomey, D. W., Onaka, P. M., et al. 2003, PASP, 115, 362
Rehemtulla, N., Fremling, C., Perley, D., & Laz, T. D. 2024a, TNSTR, 2024-2553, 1
Rehemtulla, N., Miller, A. A., Jegou Du Laz, T., et al. 2024b, ApJ, 972, 7
Rehemtulla, N., Jacobson-Galán, W. V., Singh, A., et al. 2025, ApJ, 985, 241
Reichart, D., Nysewander, M., Moran, J., et al. 2005, NCimC, 28, 767
Rest, A., Scolnic, D., Foley, R. J., et al. 2014, ApJ, 795, 44
Roming, P. W. A., Kennedy, T. E., Mason, K. O., et al. 2005, SSRv, 120, 95
Sahu, D. K., Tanaka, M., Anupama, G. C., et al. 2008, ApJ, 680, 580
Schlafly, E., Finkbeiner, D. P., & Juric, M. 2012, AAS Meeting , 219, 428.16
Schlafly, E. F., & Finkbeiner, D. P. 2011, ApJ, 737, 103
Schlawin, E., Herter, T. L., & Henderson, C. P. 2014, SPIE, 9147, 91472H
Schwab, M., Kwok, L. A., Jha, S. W., et al. 2026, ApJ, 998, 240
Science Software Branch at STScI 2012, PyRAF: Python alternative for IRAF, Astrophysics Source Code Library, ascl:1207.011
Siebert, M. R., Foley, R. J., Jones, D. O., et al. 2019, MNRAS, 486, 5785
Silverman, J. M., Foley, R. J., Filippenko, A. V., et al. 2012, MNRAS, 425, 1789
Simcoe, R. A., Burgasser, A. J., Schechter, P. L., et al. 2013, PASP, 125, 270
Singh, M., Misra, K., Sahu, D. K., et al. 2018, MNRAS, 474, 2551
Singh, M., Misra, K., Sahu, D. K., et al. 2022, MNRAS, 517, 5617
Singh, M., Sahu, D. K., Barna, B., et al. 2024, ApJ, 965, 73
Singh, M., Sahu, D. K., Dastidar, R., et al. 2023, ApJ, 953, 93
Smartt, S., Schmidt, B. P., Auchettl, K., et al. 2024, TNSCR, 2024-2588, 1
Smith, J. A., Tucker, D. L., Kent, S., et al. 2002, AJ, 123, 2121
Srivastav, S., Smartt, S. J., Huber, M. E., et al. 2022, MNRAS, 511, 2708
Srivastav, S., Smartt, S. J., Leloudas, G., et al. 2020, ApJL, 892, L24
Stahl, B. E., Zheng, W., de Jaeger, T., et al. 2019, MNRAS, 490, 3882
Steele, I. A., Smith, R. J., Rees, P. C., et al. 2004, SPIE, 5489, 679
Stetson, P. B. 1987, PASP, 99, 191
Stritzinger, M. D., Hsiao, E., Valenti, S., et al. 2014, A&A, 561, A146
Stritzinger, M. D., Valenti, S., Hoeflich, P., et al. 2015, A&A, 573, A2
Szalai, T., Vinkó, J., Sárneczky, K., et al. 2015, MNRAS, 453, 2103
Tartaglia, L., Sand, D. J., Valenti, S., et al. 2018, ApJ, 853, 62
Tinyanont, S., Foley, R. J., Taggart, K., et al. 2024, PASP, 136, 014201
Tomasella, L., Cappellaro, E., Benetti, S., et al. 2016, MNRAS, 459, 1018
Tomasella, L., Stritzinger, M., Benetti, S., et al. 2020, MNRAS, 496, 1132
Tonry, J. L., Stubbs, C. W., Lykke, K. R., et al. 2012, ApJ, 750, 99
Valenti, S., Benetti, S., Cappellaro, E., et al. 2008, MNRAS, 383, 1485
Valenti, S., Howell, D. A., Stritzinger, M. D., et al. 2016, MNRAS, 459, 3939
Valenti, S., Sand, D., Pastorello, A., et al. 2014, MNRAS, 438, L101
Vernet, J., Dekker, H., D'Odorico, S., et al. 2011, A&A, 536, A105
Wang, L. 2005, ApJL, 635, L33
Wang, X., Li, W., Filippenko, A. V., et al. 2008, ApJ, 675, 626
Ward, S. M., Thorp, S., Mandel, K. S., et al. 2023, ApJ, 956, 111
Yamanaka, M., Maeda, K., Kawabata, K. S., et al. 2015, ApJ, 806, 191
Yaron, O., & Gal-Yam, A. 2012, PASP, 124, 668
Zackay, B., Ofek, E. O., & Gal-Yam, A. 2016, ApJ, 830, 27